

1  
2  
3  
4  
5  
6  
7  
8  
9  
10  
11  
12  
13  
14  
15  
16  
17  
18  
19  
20  
21  
22

# **Probing fault frictional properties during afterslip up- and downdip of the 2017 Mw 7.3 Sarpol-e Zahab earthquake with space geodesy**

<sup>1</sup>Kang Wang and <sup>1</sup>Roland Bürgmann

<sup>1</sup> *University of California, Berkeley, Department of Earth and Planetary Sciences, Berkeley, CA 94720, USA*

## **Abstract**

We use Interferometric Synthetic Aperture Radar (InSAR) data collected by the Sentinel-1 mission to study the co- and postseismic deformation due to the 2017 Mw 7.3 Sarpol-e Zahab earthquake occurred near the Iran-Iraq border in Northwest Zagros. We find that most of the coseismic moment release is between 15 and 21 km depth, well beneath the boundary between the sedimentary cover and underlying basement. Data from all four satellite tracks also reveal robust postseismic deformation during ~ 12 months after the mainshock (from November 2017 to December 2018). Kinematic inversions show that the observed postseismic InSAR LOS displacements are well explained by oblique (thrust + dextral) afterslip both updip and downdip of the coseismic peak slip area. The dip angle of the shallow afterslip fault plane is found to be significantly smaller than that of the coseismic rupture, corresponding to a shallowly dipping detachment located near the base of the sediments. Aftershocks during the same time period exhibit a similar temporal evolution as the InSAR time series, with most of the aftershocks being located within and around the area of maximum surface deformation. The postseismic deformation data are consistent with stress-driven afterslip models, assuming that the afterslip evolution is governed by rate-strengthening friction. The preferred value of  $a\sigma$  for the updip afterslip zone is ~30-40

23 times higher than that of the downdip afterslip zone. The contrasting frictional properties updip  
24 and downdip of the coseismic rupture likely reflect differences in fault zone materials at different  
25 depths along the Zagros.

## 26 **Introduction**

27 With a total length of more than 1000 km, the Zagros Mountains in southwestern Iran are one of  
28 the major seismically active orogens in the world. The active deformation is a consequence of the  
29 ongoing continental collision between the Arabian and Eurasian plates, which initiated 10~35 Ma  
30 years ago (e.g. Hessami et al., 2001; McQuarrie et al., 2003; Pirouz et al, 2017). The current plate  
31 convergence rate is ~20-30 mm/yr, of which approximately one third is accommodated by a series  
32 of folds and thrusts within the mountain range, with the remainder being mainly accommodated  
33 by the Alborz and Greater Caucasus mountain ranges to the north (Masson et al., 2005; Vernant et  
34 al, 2004), and subduction of the South Caspian Basin further to the north (Hollingsworth et al.,  
35 2008). Shallow folding and thrusting in the Zagros involve an 8-14 km thick sedimentary cover  
36 that spans the entire Phanerozoic, overlying crystalline basement hosting seismically active thrust  
37 faults (e.g., Berberian et al., 1995). A weak detachment horizon, possibly hosting evaporites, may  
38 lie at the base of the sedimentary sequence (McQuarrie, 2004). Based on distinct characteristics of  
39 topography, geomorphology, stratigraphy, and seismicity, the Zagros range can be divided into  
40 two zones: the ~200 km wide High Zagros to the northeast that averages 1.5-2 km in elevation,  
41 and the Simply Folded Belt (SFB) that lies along the frontal part of the mountain range. The SFB  
42 is further subdivided along strike into the mountainous Lurestan and Fars arcs and the low-lying  
43 Kirkuk and Dezful embayments. Despite the relatively rapid shortening across the Zagros, there is  
44 no evidence of historical surface-rupturing earthquakes in the SFB. The largest instrumentally

45 recorded earthquakes along the Zagros were the 1972 Ghir and the 1977 Khurgu earthquakes in  
46 the Fars arc in southeastern Zagros, both of which were estimated to be  $\sim$  Mw 6.7 (Nissen et al.,  
47 2011).

48

49 On November 12, 2017 at 18:18 UTC (local time 19:18), a Mw 7.3 earthquake struck the north-  
50 western portion of the SFB in the Lurestan arc, causing a total of more than 600 fatalities in Iran  
51 and Iraq. The epicenter of this event determined by the U.S. Geological Survey (USGS) is located  
52  $\sim$ 50 km north of Sarpol-e Zahab city in Kermanshah province, and only a few kilometers east of  
53 the Iran-Iraq border. So far there is no consensus on the name of this earthquake. Following most  
54 of the published literature (Chen et al., 2018; Feng et al., 2018; Gombert et al., 2019; Nissen et al.,  
55 2019), we refer to this event as the Sarpol-e Zahab (Iran) earthquake, given that Sarpol-e Zahab is  
56 the closest community with a sizable population (over 30,000), and that most of the damage and  
57 fatalities were in this city. Focal mechanism solutions of this event indicate that this earthquake  
58 ruptured either a nearly north-south trending fault (i.e. NNW trending) that dips gently to the east,  
59 or a NW striking sub-vertical fault. Geological features around the 2017 Sarpol-e Zahab earthquake  
60 include an en echelon set of right-stepping  $\sim$ NW striking reverse faults and anticlines that are  
61 associated with shortening across a series of basement-involved blind faults, namely the Mountain  
62 Frontal Fault (MFF) and the Zagros Foreland Fault (Berberian, 1995). Although the NW trending  
63 nodal plane roughly aligns with these features (Figure 1), its near-vertical dip angle makes this  
64 fault geometry unfavorably oriented in the overall compressional stress field and inconsistent with  
65 the wide distribution of aftershocks. Therefore, the more plausible east-dipping rupture plane of  
66 the 2017 Sarpol-e Zahab earthquake does not closely align with the geologically mapped thrust  
67 faults in this region.

68

69 There have been several studies focused on the source characteristics of this earthquake with both  
70 geodetic and seismic data (e.g. Barnhart et al., 2018; Chen et al., 2018; Feng et al., 2018; Gombert  
71 et al., 2019; Nissen et al., 2019). Although there are some variations among these published  
72 rupture models, they all show that the 2017 Sarpol-e Zahab earthquake ruptured a nearly N-S  
73 trending fault with oblique thrust and dextral motion over a depth range of 12-20 km. In this study,  
74 we focus on the postseismic deformation during ~1 year after the mainshock. To ensure  
75 consistency, we first derive our own coseismic slip model for the mainshock using Sentinel-1  
76 interferograms spanning the time of the mainshock. The results regarding the fault geometry and  
77 slip distribution are overall consistent with previously published studies. We next derive the  
78 postseismic deformation time series during the first year after the mainshock. Turbulent  
79 atmospheric delay in radar propagation is a significant error source in InSAR time series analysis,  
80 which makes the measurement of low-amplitude ground motion, such as postseismic deformation,  
81 quite challenging. Previous studies using Sentinel-1 data of a similar time period concluded that  
82 the postseismic deformation months after the 2017 Sarpol-e Zahab earthquake was dominated by  
83 afterslip mainly updip of the coseismic rupture (Barnhart et al., 2018; Feng et al., 2018; Liu and  
84 Xu, 2019). In this study, we use the Common-Scene-Stacking (CSS) method (Tymofyeyeva and  
85 Fialko, 2015; Wang and Fialko, 2018) to mitigate the atmospheric noise. We show that after the  
86 atmospheric noise correction, postseismic line-of-sight (LOS) displacements derived from two  
87 Sentinel-1 ascending tracks show clear deformation both west and east of the coseismic slip  
88 contours. Both kinematic inversions and stress-driven afterslip simulations show that the observed  
89 postseismic deformation is well explained by aseismic afterslip both updip and downdip of the  
90 mainshock rupture. With the time series of postseismic InSAR measurements, we invert for the

91 frictional properties of the fault updip and downdip of the 2017 Sarpol-e Zahab coseismic rupture,  
92 assuming that the afterslip is governed by a rate-strengthening friction law. We show that distinct  
93 frictional properties of updip and downdip of the coseismic rupture are required to explain the  
94 postseismic deformation after the 2017 Sarpol-e Zahab earthquake.

## 95 **Data and Methods**

### 96 **InSAR Processing**

97 Data used in this study include LOS displacements derived from synthetic aperture radar (SAR)  
98 data from four Sentinel-1 tracks (two ascending track ASC072 and ASC174 and two descending  
99 tracks DES6 and DES79, see Figure 1 for the respective scene coverages) of the Sentinel-1 A/B  
100 satellites. The SAR data are processed with GMTSAR (Sandwell et al., 2011). All images of the  
101 respective tracks are geometrically aligned to a master image using the orbital information and a  
102 Digital Elevation Model (DEM). To remove the occasionally appearing burst discontinuities that  
103 may be attributed to satellite clock errors and/or ionospheric effects, we further refine the image  
104 alignment with the Bivariate Enhanced Spectral Diversity (BESD) method (Wang et al., 2017).  
105 The topographic phase is removed using the 1 arcsec (i.e. 30 meters) DEM derived from the Shuttle  
106 Radar Topography Mission (SRTM). The interferometric phase is unwrapped with SNAPHU  
107 (Chen and Zebker, 2001).

108  
109 For the coseismic deformation, we form interferograms with image acquisitions that are closest in  
110 time to the mainshock, which include 5 to 7 days of postseismic deformation. The coseismic LOS  
111 displacements from four different view geometries are shown in Figure 2. Because of the arid  
112 sparsely vegetated environment, the epicentral area exhibits high correlation of radar phase. LOS

113 displacements from the two ascending tracks (ASC72 and ASC174) are characterized by mainly  
114 significant range decrease southwest of the USGS epicenter, while data from the descending tracks  
115 (DES6 and DES79) show range increase near the epicenter and range decrease further to the  
116 southwest. The difference in LOS deformation patterns of ascending and descending satellite  
117 tracks is indicative of significant horizontal motion.

118

119 To reduce the noise due to atmospheric perturbations and orbital inaccuracies, we flatten the LOS  
120 displacements of each track by removing a linear trend that depends on both local topography and  
121 coordinates

122

$$123 \quad \varphi = a * x + b * y + c * h + d \quad (1)$$

124

125 where  $x$  and  $y$  are pixel coordinates along range and azimuth direction, respectively, and  $h$  is the  
126 elevation. We use pixels outside the expected earthquake deformation zone to estimate this trend.  
127 The resulting LOS displacements are then downsampled with a quad-tree curvature-based  
128 algorithm (e.g. Jónsson et al., 2002). To avoid oversampling in areas with large phase gradient due  
129 to noise (e.g. residual atmospheric noise, unwrapping errors), we perform the downsampling  
130 iteratively, using the current best-fitting model to generate the bounding coordinates of each quad-  
131 tree cell for the next iteration (Wang and Fialko, 2015). For coseismic displacement, we estimate  
132 the data covariance by examining the spatial correlation of LOS displacements in the far-field,  
133 where the range change variability is expected to be mostly from atmospheric noise. We assume  
134 that the atmospheric noise is spatially stationary and radially symmetric, so its spatial correlation  
135 depends only on the distances between observations. The resulting noise distribution function is

136 then used to build the covariance matrix of the downsampled data points, assuming that the  
137 correlation between data points decays exponentially with distance (Sudhaus and Jónsson, 2011).

138

139 In response to the earthquake, the European Space Agency (ESA) amended the observation  
140 schedule to allow for data acquisitions along each track of Sentinel-1A and -1B, leading to repeat  
141 intervals of 6-days for each satellite path over the epicentral area. By the end of January of 2019,  
142 there have been more than 70 postseismic acquisitions for all four tracks shown in Figure 1. To  
143 maintain a relatively high radar coherence, we limit the temporal baselines to be less than 50 days  
144 and the geometrical orbit baseline to be shorter than 200 meters. We construct the time series of  
145 the postseismic deformation using the Small Baseline Subset (SBAS) method (e.g. Berardino et  
146 al, 2002; Schmidt and Bürgmann, 2003).

147

148 Noise due to atmospheric perturbations between image acquisitions is one of the major limitations  
149 in InSAR measurements of low-amplitude deformation, such as the postseismic transients. To  
150 reduce the atmospheric noise, in the analysis of postseismic deformation due to the 2017 Sarpol-e  
151 Zahab earthquake, we apply the method of Common-Scene-Stacking (CSS) (Tymofyeyeva and  
152 Fialko, 2015). This method exploits the fact that interferograms sharing a common scene  
153 necessarily contain the same contribution of atmospheric delays from that acquisition. Therefore  
154 by stacking many interferograms that share a common scene, one can estimate the atmospheric  
155 phase screen (APS) of that scene, assuming that the atmospheric noise is random in time and that  
156 the tectonic deformation cancels out or can be roughly corrected for. Details of the method can be  
157 found in *Tymofyeyeva and Fialko (2015)* and *Wang and Fialko (2018)*. In order to maintain the  
158 temporal resolution in the final deformation time series, we limit the stacking stencil to be no

159 greater than 18 days on each side of the target scene, resulting in a maximum of six interferograms  
160 per stack in the case of 6-days repeat intervals. We note that the CSS method is intrinsically similar  
161 to low-pass filtering that is often adopted to suppress atmospheric noise for InSAR time series  
162 analysis (e.g., Ferretti et al., 2000; Hooper et al, 2007), however, it has a few advantages. First, the  
163 stacking is carried out in an order determined by the noise level of all images. APS of images with  
164 higher noise levels are estimated first, which are then used to correct the pertinent interferograms  
165 before proceeding to the next scene. This reduces the possible leakage of noise from very ‘bad’  
166 scenes to more quiet ones. Second, the stacking is performed on the entire image, so it is  
167 computationally quite efficient. Lastly, this method can easily deal with cases of irregular  
168 acquisition intervals, e.g. missing data in the stack.

169

170 Postseismic LOS displacement time series derived from data along the ascending track ASC72,  
171 with and without correction of atmospheric noise with CSS, are shown in Figure S3 and Figure  
172 S2, respectively. While both time series exhibit significant range decrease (i.e., movement toward  
173 the satellite) over much of the image, the results with atmospheric correction are much more  
174 coherent in time. In particular, in addition to the major zone of range decrease southwest of the  
175 coseismic rupture (i.e. updip of the coseismic rupture), a narrow band of temporally coherent range  
176 decrease is also evident south of the mainshock epicenter, with partial overlapping with the surface  
177 projection of the coseismic rupture (Figure S3). This feature, however, is not clear in the results  
178 without atmospheric correction (Figure S2). The cumulative LOS displacements for the ascending  
179 track ASC72 one year after the 2017 Mw 7.3 Sarpol-e Zahab mainshock and the corresponding  
180 time series at two selected points are shown in Figure 3 (a) and (b), respectively.

181

182 The cumulative postseismic LOS displacements along all four satellite tracks are shown in Figure  
183 4. LOS displacements of the two ascending tracks (ASC72 and ASC72) are characterized by two  
184 separate zones of significant range decrease southwest and northeast of the coseismic rupture  
185 (black contours in Figure 4). In particular, the range decrease west of the coseismic rupture is  
186 distributed across a wide area, with a maximum value exceeding 10 cm during one year after the  
187 mainshock. LOS displacements of the two descending tracks (DES6 and DES79), on the other  
188 side, are characterized by an elongated zone of range increase primarily right above the coseismic  
189 rupture, plus some relatively localized range decrease southwest of the coseismic rupture. Similar  
190 to the coseismic deformation field, the different patterns of LOS displacements between ascending  
191 and descending satellite tracks indicate that postseismic relaxation of the 2017 Sarpol-e Zahab  
192 contains significant horizontal motion.

### 193 **Modeling of coseismic deformation**

194 In this section, we invert the coseismic surface deformation data for the geometry and distribution  
195 of slip of the rupture. In our modeling, we calculate the Green's function relating a unit slip to  
196 surface displacement using the solution of a rectangular dislocation in a homogeneous elastic half-  
197 space (Okada, 1985). Fault geometry, including the fault position, strike, dip and rake angles are  
198 nonlinear parameters in the coseismic slip inversion. Thus they are often not well constrained when  
199 the data quality and/or quantity are limited, leading to a potential bias in the resulting slip  
200 distribution. To mitigate this limitation, here we first invert for the fault geometry of the 2017  
201 Sarpol-e Zahab earthquake assuming a single rectangular fault patch. Model parameters in this  
202 inversion include: the location of the fault centroid (eastward and northward shift  $(x,y)$  with respect  
203 to to the epicenter of the earthquake), and depth, length, width, strike, dip and rake, and slip  
204 magnitude of the dislocation. To quantify the uncertainty of the model parameters, we implement

205 the inversion in a Bayesian inversion framework. We assume a uniform prior distribution within a  
206 wide range for each model parameter, and a Gaussian distribution for the observation errors. We  
207 sample the model space with a *slice* sampling algorithm in Matlab (Neal 2003).

208  
209 The distribution of the model parameters that yield a comparatively high posterior probability  
210 density function (PDF) is shown in Figure 5a. Thanks to the nice coverage of InSAR observations  
211 from different look directions, most of the model parameters are tightly constrained. However, we  
212 note that the acceptable range of model parameters depends on the error functions of the input  
213 data, which we estimate using data outside the deformation area with simplified assumptions that  
214 the atmospheric noise is spatially homogeneous, isotropic, and exponentially decays with distance.  
215 The results show that the 2017 Sarpol-e Zahab earthquake rupture can be approximated by an  
216 almost north-south trending (strike = 356 degrees) fault plane that is 40 km long and 15 km wide  
217 and gently dips to the east (dip angle = 17 degree). The slip centroid is found to be at a depth of  
218 ~17 km located ~20 km southwest of the USGS epicenter. As expected, there is some trade-off  
219 between the slip magnitude and fault dimension, particularly with the fault width, and depth. A  
220 moderate trade-off also exists between the strike and rake angles. Nevertheless, all models yielding  
221 a high posterior PDF have a northerly strike angle. In particular, models with a strike angle that  
222 aligns with the overall structural trend in this area (~330 degrees) fail to correctly predict the range  
223 increase (corresponding to subsidence if there is no horizontal motion) north of the major lobe of  
224 range decrease (uplift) observed in the two ascending tracks (ASC72 and ASC174), regardless of  
225 the other parameters. The preferred strike angle of 356 degrees is 20-30 degrees from the average  
226 strike of surface expressions (i.e. folding and previously mapped faults) of this area (Figure 1).  
227 The preferred strike of the 2017 Sarpol-e Zahab rupture, however, is similar to the overall

228 orientation of the Mountain Frontal Flexure (Figure 1), a structural and topographic front that  
229 divides the Zagros SFB from its foreland basin to the SW (Emami et al., 2000; Tavani et al., 2018).  
230 The preferred fault geometry and slip direction are in good agreement with the W-phase focal  
231 mechanism determined by USGS and the moment tensor solution by gCMT (Figure 5b). Overall,  
232 surface displacements predicted by the preferred model of a single dislocation patch match the  
233 observations well (Figure S3).

234  
235 We next examine the detailed slip distribution of the 2017 Mw 7.3 Sarpol-e Zahab earthquake  
236 based on the fault geometry that is determined from the single dislocation inversion above. The  
237 ~70-km-long by 55-km-wide fault plane is divided into patches whose size gradually increases  
238 along the downdip direction to ensure a relatively uniform model resolution. Each individual patch  
239 is allowed to have a thrust and right-lateral slip component of up to 10 meters. Laplacian smoothing  
240 is applied between adjacent fault patches to avoid abrupt variations in slip. We further regularize  
241 the inversion problem by requiring no slip at the fault edges, except at the updip edge of the fault.  
242 The optimal value of the smoothness is chosen by visual inspection, such that the resulting slip  
243 model appears smooth enough without significantly deteriorating the data fitting.

244  
245 Our preferred coseismic slip model of the mainshock is shown in Figure 2b. Similar to the model  
246 of a single dislocation patch, the model allowing for spatial variation in slip is also characterized  
247 by oblique slip, with nearly equal amounts of dextral and thrust components. The distributed slip  
248 model, however, has somewhat larger slip in the southern half of the rupture. The area of prominent  
249 slip ( $>1$  m) is ~40 km long by ~17 km wide, similar to the dimension of the preferred model of the  
250 single dislocation patch. The majority of the moment release is confined in a depth range between

251 15 and 20 km, with a maximum slip of ~6.5 m at a depth of ~17 km, well beneath the estimated  
252 10-12 km thickness of sedimentary cover of this region. Assuming a shear modulus of 30 GPa,  
253 the total moment release is estimated to be  $\sim 8.9 \times 10^{20}$  Nm, corresponding to a moment magnitude  
254 of 7.26, which is in good agreement with the seismic moment. The preferred slip model predicts  
255 surface displacements that fit the observations well (Figure S3). Compared to the result with a  
256 single patch, the model with variable slip distribution yields overall better fitting to the  
257 observations, particularly in the area south of the moment centroid, where the estimated slip is  
258 larger than average.

## 259 **Modeling of postseismic deformation**

260 Commonly considered models of postseismic deformation include afterslip, poroelastic rebound,  
261 and viscoelastic relaxation. Viscoelastic relaxation takes place mainly in the lower crust and/or  
262 upper mantle, where the temperature and pressure are high enough to allow for ductile flow of  
263 rocks (Bürgmann and Dresen, 2008). The observed large surface deformation updip of the  
264 coseismic rupture indicates that the deformation source is relatively shallow, and thus unlikely to  
265 be due to viscoelastic relaxation. Published models also suggest that postseismic deformation due  
266 to deeper seated viscoelastic relaxation one year after 2017 Sarpol-e Zahab earthquake is small ( $<$   
267  $\sim 3$ mm), even when choosing rather low viscosities in the lower crust and upper mantle (Barnhart  
268 et al., 2018). We show in the supplementary material that the contribution from poroelastic  
269 rebound is also negligible ( $< 5$  mm), although the magnitude and spatial pattern of surface  
270 deformation depend on the hydraulic properties of the host rocks (i.e., porosity and hydraulic  
271 diffusivity) (Figure S5 and S6). In the next section we show that the observed postseismic  
272 deformation  $\sim 12$  months after the 2017 Sarpol-e Zahab is well explained by afterslip both updip

273 and downdip of the coseismic rupture. In addition to dominantly aseismic afterslip, large  
274 aftershocks contribute to the observed cumulative postseismic deformation. On August 25th, 2018,  
275 a Mw 6.0 aftershock occurred ~30 km southeast of the mainshock  
276 (<https://earthquake.usgs.gov/earthquakes/eventpage/us1000ghda/executive>). Three months later  
277 on 11/25/2018, another strong aftershock of Mw 6.3 occurred near the southern edge of the updip  
278 deformation zone but at ~20 km depth  
279 (<https://earthquake.usgs.gov/earthquakes/eventpage/us1000hwdw/executive>). Both events  
280 produced ~2-3 cm range changes around the respective epicenters in the cumulative postseismic  
281 deformation field (Figure 4). Focal mechanism solutions of these two aftershocks are both  
282 characterized by strike slip along nearly vertical nodal planes. The contrasting depths, rupture  
283 orientations and dip angles show that these two large aftershocks occurred on structures different  
284 from the mainshock and afterslip fault planes. To avoid a potential bias in the study of postseismic  
285 deformation processes, we mask out pixels around the epicenters of these two largest aftershocks.

## 286 **Kinematic inversion of afterslip**

287 Assuming that the observed postseismic deformation is purely due to afterslip, we invert for its  
288 spatial distribution and optimize the geometry of the fault up dip of the coseismic rupture. The  
289 cumulative LOS displacements on all four tracks shown in Figure 4 are used in the inversion. Our  
290 inversion of the afterslip distribution is based on the fault geometry that was derived from the  
291 modeling of coseismic deformation, with extensions in both strike and dip directions. To account  
292 for a possible variation in fault geometry associated with a ramp-and-flat system at the mountain  
293 front, the dip angle is allowed to vary above a certain depth (hereafter called the ‘transition’  
294 depth). The dip angle beneath this transition depth is held fixed at 17 degrees found in the  
295 coseismic modeling, while the dip angle above the transition depth is a free parameter in the

296 inversion. We varied the transition depth from 10 to 16 km at 2 km intervals. For each  
297 configuration of fault geometry, we then invert for the afterslip distribution and examine the  
298 corresponding data fitting by computing the root mean square (RMS) of the residual between  
299 model and observation, which is defined as:  $RMS = \sqrt{\frac{\sum(d-d')^2}{N}}$ , where  $d$  represents the vector of  
300 downsampled InSAR LOS displacements,  $d'$  the vector of model predictions and  $N$  the number of  
301 observations.

302  
303 Figure 6a shows the RMS of the model misfit as a function of dip angle for the shallow afterslip  
304 fault plane. One clear feature is that for all the explored transition depths, the data fitting  
305 deteriorates with an increasing dip angle of the shallow part of the fault. This suggests that the dip  
306 angle of the shallow afterslip is smaller than that of the mainshock rupture plane of 17 degrees.  
307 However, models with dip angle smaller than 10 degrees updip of the transition depth yield similar  
308 data misfit, suggesting that the data have little resolution for the dip angle smaller than 10 degrees.  
309 We therefore take a value of 5 degrees as the dip angle for the updip afterslip fault plane. We did  
310 a similar test for the dip angle downdip of the coseismic rupture, and found that a wide range of  
311 dip angles (0-25 degrees) can fit the data equally well, indicating that the data do not have sufficient  
312 sensitivity to resolve the downdip fault geometry. We therefore propose a kinked fault geometry  
313 as shown in Figure 6c, which has a dip angle of 5 degrees above 14 km and 17 degrees beneath.  
314 The preferred fault geometry is overall consistent with geological cross sections across the Zagros,  
315 which feature a sub-horizontal detachment at a depth of ~10 km that separates the Phanerozoic  
316 sediments from the underlying crystalline basement (e.g. Leturmy et al., 2010; Vergés et al., 2011).

317

318 We then invert for the distribution of the afterslip using postseismic InSAR observations from all  
319 four satellite tracks. The preferred distribution of afterslip based on this geometry is shown in  
320 Figure 7a. Similar to the coseismic slip model, the afterslip model is characterized by oblique slip  
321 containing nearly equal components of thrust and dextral motion, with distinct slip zones located  
322 both updip and downdip of the coseismic rupture. Little or no afterslip is found in the area of high  
323 coseismic slip, despite the spatial smoothing. The maximum slip updip of the coseismic rupture  
324 exceeds 0.8 m during the observation period (from a few days after the mainshock to the end of  
325 November, 2018). The inferred peak slip in the downdip afterslip zone is  $\sim 0.3$  m. The cumulative  
326 moment due to afterslip is  $2.3 \times 10^{19}$  N m, which amounts to  $\sim 20\%$  of the coseismic moment  
327 release and is equivalent to the moment of a Mw 6.84 earthquake. 74.6% of the moment release  
328 occurred on the updip section of the coseismic rupture. The moment release calculated from the  
329 inferred afterslip model is significantly higher than the aftershocks during this time period, which  
330 add up to  $3.03 \times 10^{17}$  Nm and  $3.08 \times 10^{16}$  Nm for the updip and downdip regions (delineated by  
331 pink and purple polygons in Figure 3a), respectively. This indicates that the postseismic  
332 deformation of the 2017 Sarpol-e Zahab earthquake is dominated by aseismic afterslip, which has  
333 also been observed for many other events (e.g. Hsu et al. 2006; Bürgmann et al., 2002; Perfettini  
334 et al. 2010). Nonetheless, one cannot preclude the possibility that aftershocks may locally make  
335 up a larger portion of the postseismic fault slip, which is poorly resolved in geodetic afterslip  
336 models, because of the spatial smoothing and/or other numerical regularizations involved in the  
337 inversions (Lange et al., 2014). Surface deformation predicted by the afterslip model shown in  
338 Figure 7a matches the observations well (Figure 8).

### 339 **Stress-driven afterslip simulation**

340 The kinematic inversions indicate that the observed postseismic deformation one year after the  
341 2017 Sarpol-e Zahab earthquake is well explained by afterslip both updip and downdip of the  
342 coseismic rupture. To verify whether such an afterslip model is consistent with stress changes  
343 induced by the coseismic rupture, and to explore the frictional properties of the fault, we model  
344 the afterslip assuming that the evolution of afterslip is governed by rate-and-state friction (e.g.,  
345 Marone, 1998). Rather than using the full rate-and-state equations, we assume a steady-state rate-  
346 strengthening friction without healing and slip-weakening effects. The simulation of afterslip with  
347 rate-strengthening and full rate-and-state constitutive laws only differ in the very early stage of the  
348 postseismic phase, when the cumulative afterslip is less than the critical slip distance over which  
349 the state variable evolves (Marone, 1998; Perfettini and Avouac, 2007; Barbot et al., 2009). The  
350 postseismic InSAR observations in this study started 3-5 days after the mainshock, during which  
351 the cumulative afterslip is expected to already have greatly exceeded . The rate-strengthening  
352 simplification is also supported by the high-sampling-rate GPS observations shortly after the 2016  
353 Kumamoto earthquake (Milliner et al., 2020). Under the rate-strengthening simplification, the fault  
354 slip rate at the onset of the afterslip can be expressed as (e.g., Barbot et al., 2009):

$$355 \quad V = 2V_0 \sinh \frac{\Delta\tau}{a\sigma} \quad (2)$$

356 where  $V_0$  is a reference slip rate before the coseismic shear stress change  $\Delta\tau$  is applied;  $\sigma$  is the  
357 effective normal stress on the fault; and  $a$  is a constitutive parameter representing the dependence  
358 of friction on the slip rate change. Here we have assumed that the normal stress change on the fault  
359 during an earthquake is small and negligible, compared to the shear stress change (Figure 7 c,d).  
360 We note that  $V_0$  does not correspond to the interseismic loading rate (Barbot et al., 2009; Perfettini  
361 and Avouac, 2007) , as the nucleation process and propagation of dynamic waves during the

362 rupture process may accelerate the creep rate in the afterslip zone, leading to a significantly larger  
363  $V_0$  compared to the long-term interseismic slip rate (Perfettini and Avouac, 2007).

364

365 A fault of the same geometry as in the kinematic afterslip inversion is discretized into rectangular  
366 patches of uniform size of  $\sim 4$  by 3 km. The coseismic slip model shown in Figure 5b is used to  
367 generate the coseismic stress change in a uniform elastic half-space. In the depth range between  
368 15 and 20 km, where most of the coseismic slip occurs, the stress change is negative (i.e.,  
369 represents the stress drop). To avoid back slip, the afterslip on fault patches of coseismic slip  $> 0.5$   
370 m is prescribed to be zero and afterslip is only allowed to occur on patches whose centroid depths  
371 are smaller than 15 km (updip region) or larger than 20 km (downdip region). This  
372 parameterization also implies that the fault segments laterally adjacent to the coseismic rupture are  
373 ‘locked’ and are not allowed to participate in the afterslip.

374

375 Informed by the observation that the surface deformation and seismicity downdip of the coseismic  
376 rupture seem to decay faster than the updip region (Figure 3b), we allow for different frictional  
377 properties updip and downdip of the coseismic rupture. The model thus includes four free  
378 parameters:  $V_0$  and  $a\sigma$  for both the updip and downdip regions. We perform the numerical  
379 simulations with Unicycle (Barbot et al., 2017; Barbot, 2018). We treat the simulation as an inverse  
380 problem, that is, given the surface deformation data, we solve for  $V_0$  and  $V_0$  that can best explain  
381 the data.

382

383 Different from the kinematic afterslip inversion, in which only the cumulative surface deformation  
384 is used (Figure 4), here we use the time series of postseismic LOS displacements from the two

385 ascending tracks ASC72 and ASC174, which have an overall better signal-to-noise ratio, and  
386 exhibit clear separation of surface deformation updip and downdip of the coseismic rupture. Figure  
387 8 and Figures S9-11 show that the preferred model is able to predict surface deformation of all  
388 four satellite tracks reasonably well. We uniformly downsample the InSAR LOS displacements  
389 at each postseismic epoch, and discard the data with total cumulative displacements of less than 3  
390 cm. Since the InSAR time series are referenced to the first image acquisitions 5-6 days after the  
391 mainshock, the model predicted displacement at the starting epoch is subtracted from the time  
392 series of each track. The observed time series are compared with the model predictions to draw  
393 inferences about the frictional properties of the fault that minimize the misfit. We solve the  
394 problem in a Bayesian inversion framework, assuming that data are uncorrelated in space with a  
395 uniform standard deviation of 2 cm, and that all four model parameters have uniform *a priori*  
396 distributions. Similar to the coseismic slip inversion, we sample the model space using a slice  
397 sampling algorithm (Neal, 2003).

398  
399 The evolution of model parameters during the Bayesian inversion is shown in Figure 9. We note  
400 that all four parameters converge after ~200 samples, and the converged values do not depend on  
401 the initial values. We note that the ‘samples’ shown here are only results with posterior likelihood  
402 improvement in the slice sampling.

403  
404 The models yielding low data misfit have distinct values of  $V_0$  and  $a\sigma$  for updip and downdip  
405 portions of the fault, however, there is a strong tradeoff between  $V_0$  and  $a\sigma$  (Figure 9 c and f).  
406 For the updip region, mean values of  $a\sigma$  and  $V_0$  favored by the data are 2.7 MPa and 1.42 m/yr,  
407 respectively, in significant contrast to 0.073 MPa and 0.06 m/yr for the downdip region.

408 To test if such a large difference in frictional properties is resolvable by our dataset and the  
409 inversion procedures, we run a sensitivity test. We first generate the synthetic InSAR time series  
410 using the same rate-strengthening model with  $V_0=1.5$  m/yr and  $a\sigma=1.5$  MPa for the updip part of  
411 the fault, and  $V_0=0.01$  m/yr and  $a\sigma = 0.15$  MPa for the downdip part of the fault. These values  
412 produce distinct magnitudes and temporal evolutions of surface displacements updip and downdip  
413 of the coseismic rupture, similar to the observations. Gaussian noise with a standard deviation of  
414 2 cm is added to the synthetic time series. We then invert for the model parameters:  $a\sigma$  and  $V_0$  for  
415 fault sections updip and downdip of the coseismic rupture. The results are shown in Figure S7.  
416 Similar to the inversion with real data, all four parameters converge to their respective values after  
417 ~200 iterations. The preferred values of parameters updip of the coseismic rupture, however, are  
418 slightly higher than the input ones. This is likely due to the fact that for each point we have shifted  
419 the synthetic time series (with noise) by the displacement of its first epoch, to mimic the real InSAR  
420 time series. The high degree of recovery revealed by this test indicates that with current data  
421 distribution, noise characteristics and inversion procedures, it is possible to differentiate the  
422 frictional parameters updip and downdip of the coseismic rupture.

423

424 The model with the preferred values for  $a\sigma$  and  $V_0$  shown in Figure 9 produces surface deformation  
425 matching the observations well, both in time and space (Figure 8). The comparison of cumulative  
426 and time series of surface deformation between observations and model predictions for the  
427 ascending track ASC72 is shown in Figure 10. The residuals between observations and model  
428 predictions are generally less than 3 cm, comparable to the InSAR noise. Besides the major  
429 deformation zones of range decrease, the model also predicts a modest range increase in an area  
430 close to the northern tip of the coseismic rupture. This feature, however, is not clear in the data. In

431 fact, range increase or surface subsidence at the northern tip of the fault is somewhat expected,  
432 because similar to the coseismic rupture, afterslip of the 2017 Sarpol-e Zahab earthquake is also  
433 characterized by a strong component of right-lateral strike slip, which exerts ‘pull’ to the material  
434 north of the slip area to produce subsidence at the northern end of the coseismic rupture.  
435 Alternatively, the difference between model and observations in this area could be attributed to the  
436 simplified model assumption in our simulation. Our model does not allow for along-strike  
437 variation in the frictional properties, and assumes a rate-weakening rheology over the depth range  
438 of major coseismic slip (15-20 km) to prevent any slip on fault patches on and adjacent to the  
439 rupture. In reality, some degree of afterslip may take place at the two along-strike ends of the  
440 coseismic asperity, as suggested by the kinematic afterslip inversion (Figure 7a). The model also  
441 predicts surface deformation that matches the observations of the other three InSAR tracks  
442 reasonably well (Figure 9 and Figures S8-S10).

443  
444 The cumulative afterslip predicted by the best-fitting rate-strengthening afterslip model during the  
445 InSAR observation period (from 11/17/2017 to the end of November, 2018) is shown in Figure  
446 7b. Both the slip distribution and magnitude of the stress-driven afterslip model is very similar to  
447 that based on kinematic afterslip inversion. On the other hand, both the kinematic inversion and  
448 rate-strengthening afterslip models show significantly higher afterslip updip of the coseismic  
449 rupture, compared to the afterslip downdip of the coseismic rupture, although coseismic stress  
450 changes updip and downdip of the coseismic rupture are very similar (Figure 7 c and d). This  
451 suggests that postseismic deformation during ~1 year following the 2017 Sarpol-e Zahab  
452 earthquake is indeed dominantly controlled by afterslip driven by the coseismic stress change;  
453 however, the frictional properties updip and downdip of the coseismic rupture are quite distinct.

454 Our RS model suggests that until the end of the InSAR observation period of this study, afterslip  
455 has released 76% and 93% of its total potential moment for regions updip and downdip of the  
456 coseismic rupture, respectively, assuming that the coseismic stress change will eventually be fully  
457 relaxed via afterslip. The model also suggests that during the period between the mainshock on  
458 11/12/2017 and the first SAR image acquisition on 11/17/2019, moment release from early  
459 afterslip updip of the coseismic rupture is ~ 3% of its total moment after full relaxation, whereas  
460 this value is up to 53% for the downdip region. Specifically, the model predicts a LOS  
461 displacement of up to ~3 cm for the region downdip of coseismic rupture during the time period  
462 before the first SAR image acquisition, which is comparable to the total amount of surface  
463 deformation observed in this study starting on 11/17/2017 (Figure S11). Similar to the  
464 observations, the model also shows that the surface deformation downdip of the coseismic rupture  
465 decays faster than the updip region.

466

## 467 **Discussion**

468 Our inversions of coseismic displacements due to the 2017 Mw 7.3 Sarpol-e Zahab earthquakes  
469 are generally consistent with earlier studies (e.g. Barnhart et al., 2018; Feng et al., 2018; Nissen et  
470 al., 2019; Vajedian et al., 2018; Liu and Xu, 2019). Modeling of coseismic deformation suggests  
471 that the 2017 Sarpol-e Zahab earthquake ruptured a gently east-dipping fault (~17 degrees) with  
472 significant thrust and dextral strike-slip components. The models clearly reveal that moment  
473 release occurred in a depth range between 15 and 20 km, well beneath the sediment-basement  
474 boundary at 8-14 km in this region.

475

476 Active basement faults along the Zagros have been suggested before (e.g. Berberian, 1995). One  
477 of the most important basement faults is the Mountain Frontal Fault (MFF), which controls the  
478 relatively abrupt topographic and structural variation in the foreland of the SFB (i.e., a geo-flexure  
479 known as Mountain Frontal Flexure). Although surface deformation of the 2017 Sarpol-e Zahab  
480 earthquake places tight constraints on the slip distribution and subsurface fault geometry, there is  
481 no agreement on what fault hosted the mainshock. Several studies (e.g. Barnhart et al., 2018;  
482 Vajedian et al., 2018) suggest that the 2017 Sarpol-e Zahab earthquake ruptured the MFF. *Nissen*  
483 *et al.*, (2019), on the other hand, propose that the 2017 Sarpol-e Zahab earthquake may have  
484 ruptured a previously unidentified fault, the ‘Ezgeleh-Sarpolzahab fault’, rather than the MFF.  
485 Their suggestions are primarily based on the fact that the inferred dip angles of the MFF are  
486 significantly larger than the dip angle of the 2017 Sarpol-e Zahab rupture (~17 degrees), and that  
487 slip on the MFF should be predominantly of reverse mechanism. Nevertheless, several geological  
488 cross-sections along the NW Zagros suggest that the MFF may indeed have a relatively shallow  
489 dip angle at the frontal part of the mountain range (e.g. 12-15 degrees) (e.g. Emami et al., 2010;  
490 Vergés et al, 2011), and P-wave receiver function profiles have revealed a sub-horizontal  
491 discontinuity of seismic velocity at a depth of ~10-20 km extending from the MFF to the Main  
492 Recent Fault to the northeast (Motaghi, et al., 2017; Dashti et al., 2020).

493  
494 Historically, there have been no earthquakes of magnitude greater than 7 along the Zagros. Seismic  
495 moment release in the past 100 years along the Zagros only accounts for a small fraction of the  
496 total strain accumulation determined by geodesy (Masson et al., 2005), leading to the question of  
497 how the remaining shortening across the Zagros is accommodated, particularly in the basement.  
498 Modeling of coseismic deformation of several moderate-sized earthquakes along the Zagros

499 suggests that most moderate-to-large earthquake ruptures are confined to the middle-to-lower  
500 sedimentary cover, while background microseismicity and aftershocks of those events are possibly  
501 mostly in the basement (Nissen et al, 2011, 2014). These observations led to the suggestion that  
502 crystalline basement across the Zagros shortens mostly aseismically either through aseismic fault  
503 creep accompanied by microseismicity or lower-crustal ductile deformation further to the north  
504 (e.g. Nissen et al., 2011). The basement-involved rupture manifested by the 2017 Sarpol-e Zahab  
505 earthquake indicates that at least part of the elastic strain accumulation and release along the  
506 Zagros resides in the basement, highlighting the potential of seismic hazard from basement faults  
507 along the Zagros, particularly when considering that the MFF has a total length of over 1000 km  
508 (Berberian, 1995).

509  
510 The inversion of coseismic deformation clearly shows that the 2017 Sarpol-e Zahab earthquake  
511 did not reach to the surface. Close examination of coseismic interferograms, however, reveals  
512 some localized surface deformation in the southwestern corner of the zone of high coseismic  
513 surface deformation (near the city of Qasr-e Shirin). The interferograms reveal linear features that  
514 are roughly parallel to the surface fold expressions. The largest coseismic offset in LOS direction  
515 of the ascending track A72 reaches over 6 cm (Figure 11a). Postseismic InSAR time series along  
516 profiles normal to these linear features show continued surface creep. During the one year after  
517 the mainshock, cumulative surface creep (along the LOS direction of the ascending satellite track  
518 A72) across these secondary faults exceeds 3 cm at some locations. We also note that the most  
519 prominent postseismic creep occurs on a segment that did not produce clear coseismic deformation  
520 offset (Figure 11b). There are two mechanisms that can produce localized surface deformation  
521 during coseismic strains. One is simply due to triggered slip along the secondary faults. Another

522 mechanism involves localized strain due to the reduction of elastic modulus in a fault zone with  
523 finite width (e.g. Fialko et al., 2004). Typical widths of the compliant zone inferred from geodesy,  
524 seismic guided waves and tomography range from ~100 meters to a few kilometers (Fialko et al.,  
525 2004; Li et al., 2009; Allam et al., 2014; Materna and Bürgmann, 2016). The sharp discontinuities  
526 in the coseismic deformation field, as well as the continued postseismic creep across these features,  
527 are diagnostic that the observed strain localization represents triggered slip along secondary faults,  
528 rather than the response of a compliant fault zone. The observed postseismic range changes are  
529 overall consistent with the coseismic offsets across these features. The lack of a clear signal in the  
530 data from the descending tracks across these features, however, makes the interpretation of slip  
531 sense not straightforward. Given that the area is in an overall compressional regime, it is reasonable  
532 to assume that the observed range changes correspond to triggered shallow fault slip on a series of  
533 minor reverse faults.

534

535 Postseismic deformation following the 2017 Sarpol-e Zahab earthquake has been well documented  
536 in several earlier InSAR studies (e.g., Barnhart et al., 2018; Feng et al., 2018; Liu and Xu, 2019).  
537 In these studies, afterslip was found mainly updip of the coseismic rupture, with no solid evidence  
538 of downdip afterslip. Besides the fact that previous studies only used data of shorter time span,  
539 strong atmospheric noise may have also significantly contaminated the InSAR data, preventing  
540 detection of the more subtle surface deformation due to downdip afterslip. Our InSAR time series  
541 after correcting for the atmospheric noise show that the surface deformation due to slip downdip  
542 of the coseismic rupture reaches its plateau after ~100 days, while the deformation updip of the  
543 coseismic rupture continued to increase until the end of the observation period (Figure 3b). This  
544 implies that the downdip afterslip decays faster than the updip region. We find that postseismic

545 deformation one year after the 2017 Sarpol-e Zahab earthquake is consistent with an afterslip  
546 model with slip concentrated in both updip and downdip fault sections adjoining the coseismic  
547 rupture. Little afterslip is resolved in the area of high coseismic slip. The 2017 Sarpol-e Zahab  
548 earthquake is therefore a rare case, for which the distribution of afterslip largely follows the  
549 predictions from the classical model of a velocity-weakening rupture asperity clearly separated  
550 from velocity-strengthening fault sections. This may be partially attributed to the high-quality  
551 InSAR data derived in this study, which significantly improves the model resolution.

552  
553 Afterslip has been observed following many moderate to large earthquakes in different  
554 seismotectonic settings. It represents the response of faults to the stress changes induced by the  
555 coseismic rupture (e.g., Bürgmann, 2018). In the framework of rate-and-state friction, earthquakes  
556 nucleate in regions of velocity weakening frictional properties, whereas afterslip occurs on fault  
557 sections of velocity strengthening behavior away from the rupture) (Marone, 1998; Avouac, 2015).  
558 In this framework, afterslip is expected to mainly occur at the periphery of the coseismic rupture,  
559 where the rock friction is velocity strengthening and arrests the seismic rupture. A transition to  
560 velocity-strengthening behavior is expected at the down-dip portion of seismogenic faults due to  
561 increased temperature and pressure (e.g., Marone, 1998). In the upper crust, however, velocity-  
562 strengthening fault properties appear limited to specific mineralogies (e.g., clays, serpentinite,  
563 talc), macro- and microstructures (e.g., compositional heterogeneity, foliated gouge, veins),  
564 deformation mechanisms (e.g., pressure-solution creep, granular flow), and/or conditions (e.g.,  
565 near-lithostatic fluid pressure) (e.g., Bürgmann, 2018 and references cited therein). A sharp  
566 separation between coseismic slip and afterslip, however, is rarely observed, and afterslip is often  
567 inferred to substantially overlap with coseismic ruptures (e.g., Avouac, 2015 and references cited

568 therein)- In addition to the limits of resolution of geodetic inversions, another likely explanation  
569 involves the role of small-scale spatial (Johnson et al., 2006) or temporal (Hearn et al., 2012)  
570 variations in frictional parameters across the fault surface. Numerical simulations have suggested  
571 that seismic ruptures could indeed propagate into velocity-strengthening fault areas, when the fault  
572 is dynamically weakened by rapid shear heating of pore fluids (Noda and Lapusta, 2013). In such  
573 a scenario, one would expect some degree of overlap between afterslip and coseismic rupture.

574

575 While afterslip downdip of large earthquake ruptures appears common, what is the cause of  
576 velocity-strengthening fault properties updip of the 2017 Sarpol-e Zahab earthquake? Our  
577 modeling demonstrates that postseismic deformation in the updip region of the coseismic rupture  
578 likely originates from aseismic slip on a sub-horizontal plane (dip angle <10 degrees) at a depth  
579 of 12-14 km. The distinct characteristics of coseismic slip and afterslip due to the event may be  
580 related to the specific lithological and structural architecture in the Zagros. Much of the Zagros  
581 contains an 8-14 km thick Phanerozoic sedimentary cover, with the oldest basal unit being the late  
582 Proterozoic to early Cambrian Hormuz evaporites on top of the underlying crystalline basement.  
583 Although there is no firm evidence for basal Hormuz salt deposits in the northwestern SFB,  
584 mechanical considerations point to an equivalent decompling horizon in the Lurestan arc that  
585 allows for the deformation front to advance southwestward over the Arabian plate (e.g.,  
586 McQuarrie, 2004; Vergés et al., 2011). Such a mechanically weak layer may act as a barrier to  
587 prevent seismic events that nucleated in the sedimentary cover from propagating into the basement,  
588 and vice versa. In our modeling, we assume that postseismic deformation following the 2017  
589 Sarpol-e Zahab earthquake is dominantly controlled by afterslip following a rate-strengthening  
590 friction; however, ductile shearing of the evaporite layer may have relieved the stress change from

591 the Sarpol-e Zahab rupture. Although mechanically afterslip and ductile shearing are different  
592 behaviors, it has been shown that crystal-plastic flow within a finite-width shear zone following a  
593 power-law dependence of strain rate on stress is mathematically equivalent to afterslip following  
594 a rate-and-state frictional law (e.g. Perfettini and Avouac, 2004; Barbot et al., 2009). This scenario  
595 is consistent with the previous inference that any slip taking place between the metamorphic  
596 basement and the overlying sedimentary cover above the Hormuz salt is aseismic (Berberian,  
597 1995). The unique lithological structure of the Zagros could also explain why the afterslip  
598 distribution following the 2017 Sarpol-e Zahab earthquake significantly differ from other thrust  
599 events of similar magnitudes and tectonic settings; e.g., the 1999 Chi-Chi, the 2003 Chengkung,  
600 the 2005 Kashmir, and the 2015 Gorkha earthquakes, where afterslip years after the mainshock  
601 was all found predominantly downdip of the coseismic rupture (e.g. Hsu et al, 2002, 2009; Wang  
602 and Fialko, 2014, 2018; Zhao et al., 2017).

603

604 Accompanying the afterslip, the 2017 Sarpol-e Zahab earthquake also produced a large number of  
605 aftershocks during the InSAR observation period. Despite the relatively poor locations of  
606 earthquakes in the Zagros, the current earthquake catalog shows that most of the aftershocks in the  
607 first year after the 2017 Sarpol-e Zahab mainshock surround the area of high coseismic slip (Figure  
608 5b and 7). This is somewhat expected, because of the stress increase at the periphery of the  
609 coseismic rupture (Figure 7c-d). The mechanisms of aftershocks, particularly their relationship  
610 with postseismic deformation processes, however, remains unclear. One popular model suggests  
611 that aftershocks result from the direct effect of coseismic stress change on a population of  
612 nucleating faults with a rate-weakening rheology (Dieterich 1994). In this model, aftershocks and  
613 afterslip are not expected to follow the same temporal evolution, as they represent different

614 physical responses to the coseismic stress change. On the other hand, it has been suggested that  
615 aftershocks represent velocity-weakening asperities embedded in a dominantly velocity-  
616 strengthening fault and are directly triggered by afterslip, thus they share similar spatial and  
617 temporal evolution patterns (Perfettini & Avouac, 2004; Perfettini et al., 2018). In this study, we  
618 show that the aftershocks and surface displacements both updip and downdip of the coseismic  
619 rupture follow similar temporal patterns, suggesting that afterslip may indeed have played a direct  
620 role in driving the occurrence of aftershocks.

621

622 In this study, we estimate the frictional properties of the VS fault sections that experience afterslip  
623 in the rate-and-state framework using the surface deformation data. As shown in equation (1),  
624 under the rate-strengthening simplification, the slip rate at the onset of afterslip depends on initial  
625 slip rate  $v_0$ , the dependence of friction on slip rate change  $a$  and the effective normal stress  $\sigma$ , and the  
626 coseismic stress change  $\Delta\sigma$ . There are different explanations about the physical meaning of  $a$ . Some  
627 authors suggest that  $a$  should be thought of as a rock property that controls the timescale of afterslip,  
628 so it has nothing to do with the actual pre-earthquake fault slip history (e.g. Bartbot et al., 2009).  
629 In contrast, others suggest that  $v_0$  should be the pre-earthquake slip rate (e.g. Johnson et al., 2006;  
630 Perfettini and Avouac 2007). Since equation (2) is a general expression of fault slip rate based on  
631 the rate-and-state frictional law, which relates the coefficient of friction to the sliding velocity of  
632 the slider in a spring-slider system, the ‘initial’ velocity  $v_0$  on the right-hand side of the equation  
633 should be the fault slip rate right before the coseismic shear stress change is applied, i.e., the pre-  
634 earthquake slip rate. However, due to the earthquake nucleation, dynamic stress perturbation and  
635 weakening, and external loading from viscoelastic relaxation shortly after the earthquake, the slip  
636 rate right before the occurrence of afterslip shown in equation (1) could exceed the interseismic

637 slip rate over a longer period (Perfettini and Avouac 2007). Therefore, instead of assuming to be  
638 the same as the interseismic slip rate (e.g. Johnson et al., 2006), we leave it as a free parameter.

639  
640 The results show a strong tradeoff between  $\lambda$  and  $V_0$ . For a wide range of tested values that yield  
641 relatively good fitting to the observations, the distribution of  $\lambda$  seems to be linearly correlated with  $V_0$ .  
642 This is somewhat expected, as for small value of  $\lambda$ . Despite the strong tradeoff between  $\lambda$  and  $V_0$ , all  
643 the models yielding acceptable data fitting prefer a relatively high value of  $V_0$  (on the order of m/yr).  
644 Specifically, the model that yields the best-fitting LOS displacement time series for the ascending  
645 track ASC72 has  $\lambda$  for the updip section of the fault. This is substantially higher than the overall  
646 convergence rate of <15 mm/yr across the Zagros (Hessami et al., 2006; Vernant et al., 2004),  
647 which is further partitioned between multiple faults and folds in the mountain range. To test if such  
648 a large value of  $\lambda$  is required by the data, we run another test by setting, a velocity comparable to the  
649 interseismic slip rate across the faults in the SFB. We find that the model with such a small value  
650 of initial velocity  $V_0$  would significantly underpredict the surface deformation updip of the coseismic  
651 rupture, regardless of other parameters.

652  
653 High values of  $V_0$  have also been documented in the modeling of the postseismic GPS data  
654 following the 1992 Landers earthquake (Perfettini and Avouac 2007), in which the preferred  
655 initial velocity is as large as 100 mm/yr. What causes such large pre-earthquake slip rates before  
656 the Landers and the 2017 Sarpol-e Zahab earthquakes remains unclear. In addition to the  
657 possibilities (e.g. earthquake nucleation, dynamic stress perturbation, loading from underneath  
658 viscoelastic relaxation shortly after the earthquake) discussed in *Perfettini and Avouac (2007)*,  
659 foreshock excitation might be another effective way to enhance the fault slip rate leading to the

660 mainshock. For the 2017 Sarpol-e Zahab earthquake, a series of  $M_L$  4-5 earthquakes had occurred  
661 within a few hours before the Mw 7.3 mainshock, with the closest one being only ~43 mins before  
662 mainshock (Nissen et al., 2019). It is possible that the stress change from these aftershocks  
663 enhanced the creep rate on the fault portions with velocity-strengthening friction, leading to a  
664 higher value  $V_0$  of compared to the long-term interseismic creep rate.

## 665 **Conclusions**

666 With more than 600 fatalities in Iran and Iraq, the 2017 Mw 7.3 Sarpol-e Zahab earthquake was  
667 the largest instrumentally recorded seismic event along the Zagros mountain range. Similar to most  
668 previous large earthquakes along the Zagros, the 2017 Sarpol-e Zahab earthquake did not break to  
669 the surface, making the interpretation of its seismogenic structure elusive. In this study, we use  
670 Sentinel-1 InSAR to study the co- and postseismic deformation due to this event. Thanks to the  
671 arid environment and sparse vegetation in the epicentral area, both the coseismic and postseismic  
672 deformation of the 2017 Sarpol-e Zahab earthquake are well imaged by Sentinel-1 InSAR  
673 observations from four different look directions, which allowed us to tightly constrain the fault  
674 geometry and slip distribution of the 2017 Sarpol-e Zahab earthquake. We find that even though  
675 most surface expressions (i.e., faults and folds) in this area trend in a northwest-southeast direction,  
676 the 2017 Sarpol-e Zahab event ruptured a nearly north-south trending plane (strike = 356 degrees)  
677 that gently dips to the east (dip angle = 17 degrees). The coseismic rupture is characterized by  
678 nearly equal amounts of thrust and dextral motion distributed on a ~40-km-long and 15-km-wide  
679 fault plane, with most of the seismic moment release concentrated in a depth range between 15  
680 and 21 km, which is beneath the boundary between the Phanerozoic sedimentary cover and

681 underlying Proterozoic basement. The 2017 Sarpol-e Zahab earthquake therefore highlights the  
682 importances of basement faults in accommodating crustal shortening across the Zagros.  
683  
684 Data from all four Sentinel-1 tracks also reveal robust postseismic deformation during ~12 month  
685 after the mainshock. We have shown that with appropriate corrections for atmospheric noises, the  
686 Sentinel-1 InSAR data clearly reveal postseismic deformation both to the west and east of the  
687 coseismic rupture, whereas previous studies with similar data only identified the western zone.  
688 Kinematic inversions show that the observed postseismic InSAR LOS displacements are well  
689 explained by oblique (thrust + dextral) afterslip both updip and downdip of the coseismic slip area.  
690 The dip angle of the shallow afterslip fault plane is found to be significantly smaller than that of  
691 the coseismic rupture, corresponding to a shallowly dipping detachment located near the base of  
692 the sediments. The postseismic deformation data are consistent with stress-driven afterslip models,  
693 assuming that the afterslip evolution is governed by rate-and-state friction. Assuming a rate-  
694 strengthening friction, the preferred value of  $\alpha$  for the updip afterslip zone is ~30-40 times  
695 higher than that of the downdip afterslip zone. The contrast in the frictional properties updip and  
696 downdip of the coseismic rupture is likely attributed to the difference in fault zone materials and  
697 physical conditions at different depths along the Zagros. In particular, the up-dip afterslip occurs  
698 along a sub-horizontal plane at a depth of ~12-14 km, which could be related to the Cambrian  
699 Hormoz evaporite deposit layer that behaves as a mechanically weak layer to decouple the  
700 deformation of underlying crystalline basement from above. In contrast, afterslip downdip of the  
701 coseismic rupture may be mostly controlled by the increased temperature and pressure, which  
702 favor stable sliding, as has been found in other continental earthquakes of similar tectonic settings.  
703

704 **Acknowledgement**

705 Sentinel- 1 data are copyright of European Space Agency (ESA) and archived and distributed by  
706 Alaska Satellite Facility (ASF). The Common-Scene-Stacking code used to mitigate the InSAR  
707 atmospheric noise is available from the authors upon request. Aftershock catalog used in this  
708 study are from Iranian Seismic Center (ISC) (<http://irsc.ut.ac.ir/>). We thank Sylvain Barbot for  
709 sharing and assisting on the software package Unicycle. This work benefited from discussions  
710 and email exchanges with Sylvain Barbot, Jean-Philippe Avouac and Hugo Perfettini. This work  
711 is supported by supported by the NASA Earth Surface and Interior award NNX16AL17G.

712 **References**

713 Allam, A. A., Y. Ben-Zion, I. Kurzon, and F. Vernon (2014), Seismic velocity structure in the Hot  
714 Springs and Trifurcation areas of the San Jacinto fault zone, California, from double-difference  
715 tomography, *Geophysical Journal International*, 198(2), 978–999, doi:10.1093/gji/ggu176.

716

717 Allen, M. B., Saville, C., Blanc, E. J.-P., Talebian, M., & Nissen, E. (2013). Orogenic plateau  
718 growth: Expansion of the Turkish-Iranian Plateau across the Zagros fold-and-thrust belt. *Tectonics*,  
719 32(2), 171–190, doi:10.1002/tect.20025.

720

721 Barbot, S., Fialko, Y., & Bock, Y. (2009). Postseismic deformation due to the Mw6.0 2004  
722 Parkfield earthquake: Stress-driven creep on a fault with spatially variable rate-and-state friction  
723 parameters. *Journal of Geophysical Research*, 114(B7), 1279, doi:10.1029/2008JB005748.

724

725 Barnhart, W. D., & Lohman, R. B. (2013). Phantom earthquakes and triggered aseismic creep:  
726 Vertical partitioning of strain during earthquake sequences in Iran. *Geophysical Research Letters*,  
727 40(5), 819–823, doi:10.1002/grl.50201.

728

729 Barnhart, W. D., Brengman, C. M. J., Li, S., & Peterson, K. E. (2018). Ramp-flat basement  
730 structures of the Zagros Mountains inferred from co-seismic slip and afterslip of the 2017 M w 7.3  
731 Darbandikhan, Iran/Iraq earthquake. *Earth and Planetary Science Letters*, 496, 96-107,  
732 doi:10.1016/j.epsl.2018.05.036.

733

734 Barbot, S., Moore, J. D. P., & Lambert, V. (2017). Displacement and Stress Associated with  
735 Distributed Anelastic Deformation in a Half-Space. *Bulletin of the Seismological Society of*  
736 *America*, 107(2), 821–855, doi:10.1785/0120160237.

737  
738 Barbot, S. (2018). Asthenosphere Flow Modulated by Megathrust Earthquake Cycles. *Geophysical*  
739 *Research Letters*, 118(1), 3059-14. <http://doi.org/10.1029/2018GL078197>

740 Berberian, M. (1995). Master “blind” thrust faults hidden under the Zagros folds: active basement  
741 tectonics and surface morphotectonics. *Tectonophysics*, 241(3-4), 193-224, doi:10.1016/0040-  
742 1951(94)00185-C.

743  
744 Berardino, P., & Fornaro, G. (2002). A new algorithm for surface deformation monitoring based  
745 on small baseline differential SAR interferograms, *IEEE Transactions on Geoscience and*  
746 *Remote Sensing*, 40(11), 2375-2383, doi:10.1109/TGRS.2002.803792.

747  
748 Berberian, M. (1995). Master “blind” thrust faults hidden under the Zagros folds: active basement  
749 tectonics and surface morphotectonics. *Tectonophysics*, 241(3-4), 193–224, doi:10.1016/0040-  
750 1951(94)00185-C.

751  
752 Bürgmann, R., Ergintav, S., Segall, P., Hearn, E. H., McClusky, S., Reilinger, R., et al. (2002).  
753 Time-dependent distributed afterslip on and deep below the Izmit earthquake rupture. *Bulletin of*  
754 *the Seismological Society of America*, 92(1), 126–137, doi:10.1785/0120000833.

755

756 Bürgmann, R., and G. Dresen (2008), Rheology of the Lower Crust and Upper Mantle: Evidence  
757 from Rock Mechanics, Geodesy, and Field Observations, *Annual Review of Earth and Planetary*  
758 *Sciences*, 36(1), 531–567, doi:10.1146/annurev.earth.36.031207.124326.

759  
760 Bürgmann, R. (2018). The geophysics, geology and mechanics of slow fault slip. *Earth and*  
761 *Planetary Science Letters*, 495, 112–134, doi:10.1016/j.epsl.2018.04.062.

762  
763 Chang, S.-H., Avouac, J.-P., Barbot, S., & Lee, J.-C. (2013). Spatially variable fault friction  
764 derived from dynamic modeling of aseismic afterslip due to the 2004 Parkfield earthquake.  
765 *Journal of Geophysical Research: Solid Earth*, 118(7), 3431–3447, doi:10.1002/jgrb.50231.

766  
767 Dashti, F., F. P. Lucente, K. Motaghi, I. Bianchi, M. Najafi, A. Govoni, and E. Shabanian (2020),  
768 Crustal Scale Imaging of the Arabia-Central Iran Collision Boundary Across the Zagros Suture  
769 Zone, West of Iran, *Geophysical Research Letters*, 47(8), 1395, doi:10.1029/2019GL085921.

770  
771 Elliott, J. R., Bergman, E. A., Copley, A. C., Ghods, A. R., Nissen, E., Oveisi, B., et al. (2015).  
772 The 2013 Mw 6.2 Khaki-Shonbe (Iran) Earthquake: Insights into seismic and aseismic shortening  
773 of the Zagros sedimentary cover. *Earth and Space Science*, 2, 435-471,  
774 doi:10.1002/2015EA000098.

775  
776 Emami, H., Vergés, J., Nalpas, T., Gillespie, P., Sharp, I., Karpuz, R., et al. (2010). Structure of  
777 the Mountain Front Flexure along the Anaran anticline in the Pusht-e Kuh Arc (NW Zagros, Iran):

778 insights from sand box models. *Geological Society, London, Special Publications*, 330(1), 155–  
779 178, doi:10.1144/SP330.9.

780

781

782 Feng, W., Samsonov, S., Almeida, R., Yassaghi, A., & Zheng, W. (2018). Geodetic Constraints of  
783 the 2017 Mw7.3 Sarpol Zahab, Iran Earthquake, and Its Implications on the Structure and

784 Fielding, E. J., Wright, T. J., Muller, J., Parsons, B. E., & Walker, R. (2004). Aseismic deformation  
785 of a fold-and-thrust belt imaged by synthetic aperture radar interferometry near Shahdad, southeast  
786 Iran. *Geology*, 32(7), 577, doi:10.1130/G20452.1.

787

788 Ferretti, A., Prati, C., & Racca, F. (2000). Nonlinear subsidence rate estimation using permanent  
789 scatterers in differential SAR interferometry. *IEEE Transactions on Geoscience and Remote*  
790 *Sensing*, 38(5), 2202–2212.

791

792 Fialko, Y., Sandwell, D., Agnew, D., Simons, M., Shearer, P., & Minster, B. (2002). Deformation  
793 on Nearby Faults Induced by the 1999 Hector Mine Earthquake. *Science*, 297(5588), 1858–1862,  
794 doi:10.1126/science.1074671.

795

796

797 Hearn, E. H., Bürgmann, R., & Reilinger, R. E. (2002). Dynamics of Izmit earthquake postseismic  
798 deformation and loading of the Duzce earthquake hypocenter. *Bulletin of the Seismological Society*  
799 *of America*, 92(1), 172–193, doi:10.1785/0120000832.

800

801 Hollingsworth, J., Jackson, J., Walker, R., & Nazari, H. (2008). Extrusion tectonics and subduction  
802 in the eastern South Caspian region since 10 Ma. *Geology*, 36(10), 763–4,  
803 doi:10.1130/G25008A.1.

804

805 Hooper, A., Bechor, N., & Zebker, H. (2007). Persistent scatterer interferometric synthetic aperture  
806 radar for crustal deformation analysis, with application to Volcán Alcedo, Galápagos. *Journal of*  
807 *Geophysical Research*, 112(B7), B07407–21, doi:10.1029/2006JB004763.

808

809

810 Hsu, Y.-J., Bechor, N., Segall, P., Yu, S.-B., Kuo, L.-C., & Ma, K.-F. (2002). Temporal and spatial  
811 variations of post-seismic deformation following the 1999 Chi-Chi, Taiwan earthquake.  
812 *Geophysical Research Letters*, 29(16), doi:10.1029/2002GL014967

813

814 Hsu, Y.-J., M. Simons, J.-P. Avouac, J. Galetzka, K. Sieh, M. Chlieh, D. Natawidjaja, L.  
815 Prawirodirdjo, and Y. Bock (2006), Frictional afterslip following the 2005 Nias-Simeulue  
816 earthquake, Sumatra, *Science*, 312(5782), 1921–1926, doi:10.1126/science.1126960.

817

818 Hsu, Y.-J., S. B. Yu, and H.-Y. Chen (2009), Coseismic and postseismic deformation associated  
819 with the 2003 Chengkung, Taiwan, earthquake, *Geophysical Journal International*, 176(2), 420–  
820 430, doi:10.1111/j.1365-246X.2008.04009.x.

821 Hessami, K., Koyi, H. A., Talbot, C. J., Tabasi, H., & Shabanian, E. (2001). Progressive  
822 unconformities within an evolving foreland fold–thrust belt, Zagros Mountains. *Journal of the*  
823 *Geological Society*, 158(8), 969–981, doi:10.1144/0016-764901-007.

824

825 Jónsson, S., H. Zebker, P. Segall, and F. Amelung (2002). Fault slip distribution of the 1999 Mw  
826 7.1 Hector Mine, California, earth- quake, estimated from satellite radar and GPS measurements,  
827 *Bull. Seismol. Soc. Am.* 92, no. 4, 1377–1389, doi: 10.1785/0120000922.

828

829 Lange, D., J. R. Bedford, M. Moreno, F. Tilmann, J. C. Baez, M. Bevis, and F. Krüger (2014),  
830 Comparison of postseismic afterslip models with aftershock seismicity for three subduction-zone  
831 earthquakes: Nias 2005, Maule 2010 and Tohoku 2011, *Geophysical Journal International*,  
832 199(2), 784–799, doi:10.1093/gji/ggu292.

833 Leturmy, P., Molinaro, M., & de Lamotte, D. F. (2010). Structure, timing and morphological  
834 signature of hidden reverse basement faults in the Fars Arc of the Zagros (Iran). *Geological Society*  
835 *Special Publication*, 330, 121–138, doi:10.1144/SP330.7.

836 Li, Y. G., P. Leary, K. Aki, and P. Malin (1990), Seismic Trapped Modes in the Oroville and San  
837 Andreas Fault Zones, *Science*, 249(4970), 763–766, doi:10.1126/science.249.4970.763.

838 Liu, X., and W. Xu (2019), Logarithmic Model Joint Inversion Method for Coseismic and  
839 Postseismic Slip: Application to the 2017 Mw 7.3 Sarpol Zahāb Earthquake, Iran, *Journal of*  
840 *Geophysical Research: Solid Earth*, 2019JB017953, doi:10.1029/2019JB017953.

841

842 McQuarrie, N., Stock, J. M., Verdel, C., & Wernicke, B. P. (2003). Cenozoic evolution of  
843 Neotethys and implications for the causes of plate motions. *Geophysical Research Letters*, 30(20),  
844 doi:10.1029/2003GL017992.

845

846 Masson, F., Chéry, J., Hatzfeld, D., Martinod, J., Vernant, P., Tavakoli, F., & Ashtiani, M. G.  
847 (2005). Seismic versus aseismic deformation in Iran inferred from earthquakes and geodetic data.  
848 *Geophysical Journal International*, 160(1), 217–226, doi:10.1111/j.1365-246X.2004.02465.x.  
849

850 McQuarrie, N. (2004). Crustal scale geometry of the Zagros fold–thrust belt, Iran  
851 . *Journal of Structural Geology*, 26, 519–535.  
852

853 Motaghi, K., Shabanian, E., & Kalvandi, F. (2017). Underplating along the northern portion of the  
854 Zagros suture zone, Iran. *Geophysical Journal International*, 210(1), 375–389,  
855 doi:10.1093/gji/ggx168.  
856

857 Neal, R. M. (2003). Slice sampling. *Annals of Statistics*, doi:10.1214/aos/1056562461.

858 Noda, H., & Lapusta, N. (2013). Stable creeping fault segments can become destructive as a result  
859 of dynamic weakening. *Nature*, 493(7433), 518–521, doi:10.1038/nature11703.  
860

861 Nissen, E., Yamini-Fard, F., Tatar, M., Gholamzadeh, A., Bergman, E., Elliott, J. R., et al. (2010).  
862 The vertical separation of mainshock rupture and microseismicity at Qeshm island in the Zagros  
863 fold-and-thrust belt, Iran. *Earth and Planetary Science Letters*, 296(3), 181–194,  
864 doi:10.1016/j.epsl.2010.04.049.  
865

866 Nissen, E., Tatar, M., Jackson, J. A., & Allen, M. B. (2011). New views on earthquake faulting in  
867 the Zagros fold-and-thrust belt of Iran. *Geophysical Journal International*, 186(3), 928–944,  
868 doi:10.1111/j.1365-246X.2011.5119.x.

869

870 Okada, Y. (1985). Surface deformation due to shear and tensile faults in a half-space. *Bulletin of*  
871 *the Seismological Society of America*, 75(4), 1135-1154.

872

873 Perfettini, H., & Avouac, J. P. (2004). Postseismic relaxation driven by brittle creep: A possible  
874 mechanism to reconcile geodetic measurements and the decay rate of aftershocks, application to  
875 the Chi-Chi earthquake, Taiwan. *Journal of Geophysical Research: Solid Earth (1978–2012)*,  
876 109(B2), 4005, doi:10.1029/2003JB002488.

877

878 Perfettini, H., & Avouac, J. P. (2007). Modeling afterslip and aftershocks following the 1992  
879 Landers earthquake. *Journal of Geophysical Research: Solid Earth*, 112(B07409), 2433,  
880 doi:10.1029/2006JB004399.

881

882 Perfettini, H. et al. (2010), Seismic and aseismic slip on the Central Peru megathrust, *Nature*,  
883 465(7294), 78–81, doi:10.1038/nature09062.

884

885 Perfettini, H., Frank, W. B., Marsan, D., & Bouchon, M. (2018). A model of aftershock migration  
886 driven by afterslip. *Geophysical Research Letters*, 45, 2283–2293, doi:10.1002/2017GL076287.

887

888 Pirouz, M., Avouac, J.-P., Hassanzadeh, J., Kirschvink, J. L., & Bahroudi, A. (2017). Early  
889 Neogene foreland of the Zagros, implications for the initial closure of the Neo-Tethys and  
890 kinematics of crustal shortening. *Earth and Planetary Science Letters*, 477, 168-182,  
891 doi:10.1016/j.epsl.2017.07.046.

892

893 Ruina, A. (2012). Slip instability and state variable friction laws. *Journal of Geophysical Research*,  
894 88(B12), 10359-10370, doi:10.1029/JB088iB12p10359.

895

896 Scholz, C. H. (1998). Earthquakes and friction laws. *Nature Publishing Group*, 391(6662), 37–42,  
897 doi:10.1038/34097.

898

899 Sudhaus, H., & Jónsson, S. (2009). Improved source modelling through combined use of InSAR  
900 and GPS under consideration of correlated data errors: application to the June 2000 Kleifarvatn  
901 earthquake, Iceland. *Geophysical Journal International*, 176(2), 389-404, doi:10.1111/j.1365-  
902 246X.2008.03989.x.

903

904 Tavani, S., M. Parente, F. Puzone, A. Corradetti, G. Gharabeigli, M. Valinejad, D. Morsalnejad,  
905 and S. Mazzoli (2018), The seismogenic fault system of the 2017 Mw 7.3 Iran-Iraq earthquake:  
906 constraints from surface and subsurface data, cross-section balancing, and restoration, *Solid Earth*,  
907 9(3), 821–831, doi:10.5194/se-9-821-2018.

908

909 Tymofyeyeva, E., & Fialko, Y. (2015). Mitigation of atmospheric phase delays in InSAR data,  
910 with application to the eastern California shear zone. *Journal of Geophysical Research: Solid*  
911 *Earth*, 120(8), 5952-5963, doi:10.1002/2015jb011886.

912

913 Wang, K., & Fialko, Y. (2014). Space geodetic observations and models of postseismic  
914 deformation due to the 2005 M7.6 Kashmir (Pakistan) earthquake. *Journal of Geophysical*  
915 *Research: Solid Earth*, 119(9), 7306–7318, doi:10.1002/2014JB011122.

916

917 Wang, K., & Fialko, Y. (2015). Slip model of the 2015 M-w 7.8 Gorkha (Nepal) earthquake from  
918 inversions of ALOS-2 and GPS data. *Geophysical Research Letters*, 42(18), 7452-7458,  
919 doi:10.1002/2015GL065201.

920

921 Wang, K., Xu, X., & Fialko, Y. (2017). Improving Burst Alignment in TOPS Interferometry With  
922 Bivariate Enhanced Spectral Diversity. *IEEE Geoscience and Remote Sensing Letters*, 14(12),  
923 2423-2427, doi:10.1109/LGRS.2017.2767575.

924

925 Wang, K., & Fialko, Y. (2018). Observations and Modeling of Coseismic and Postseismic  
926 Deformation Due To the 2015 Mw 7.8 Gorkha (Nepal) Earthquake. *Journal of Geophysical*  
927 *Research: Solid Earth*, 123(1), 761-779, doi:10.1002/2017JB014620.

928

929 Vajedian, S., Motagh, M., Mousavi, Z., Motaghi, K., Fielding, E., Akbari, B., et al. (2018).  
930 Coseismic Deformation Field of the Mw 7.3 12 November 2017 Sarpol-e Zahab (Iran) Earthquake:  
931 A Decoupling Horizon in the Northern Zagros Mountains Inferred from InSAR Observations.  
932 *Remote Sensing*, 10(10), 1589, doi:10.3390/rs10101589.

933

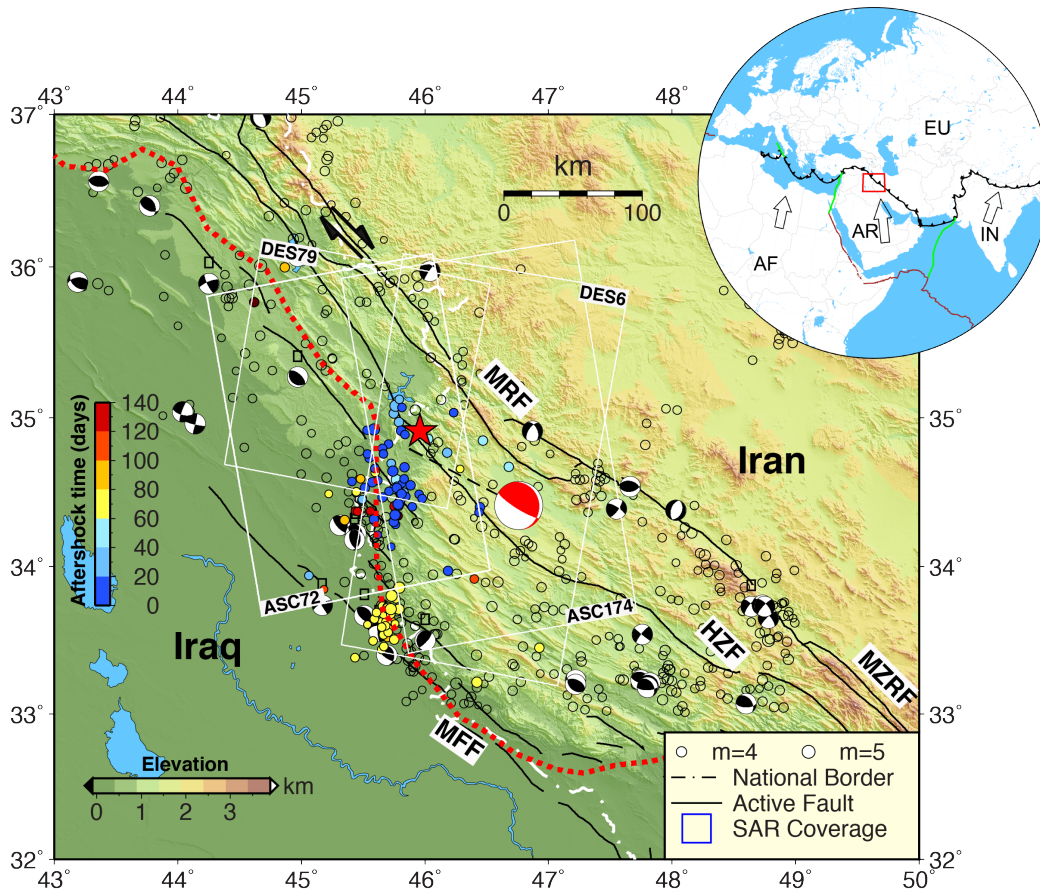
934 Vernant, P., Nilforoushan, F., Hatzfeld, D., Abbassi, M. R., Vigny, C., Masson, F., et al. (2004).  
935 Present-day crustal deformation and plate kinematics in the Middle East constrained by GPS

936 measurements in Iran and northern Oman. *Geophysical Journal International*, 157(1), 381–398,  
937 doi:10.1111/j.1365-246X.2004.02222.x.

938

939 Vergés, J., Saura, E., Casciello, E., Fernàndez, M., Villaseñor, A., Jiménez-munt, I., & García-  
940 castellanos, D. (2011). Crustal-scale cross-sections across the NW Zagros belt: implications for  
941 the Arabian margin reconstruction. *Geological Magazine*, 148(5-6), 739–761,  
942 doi:10.1017/S0016756811000331.

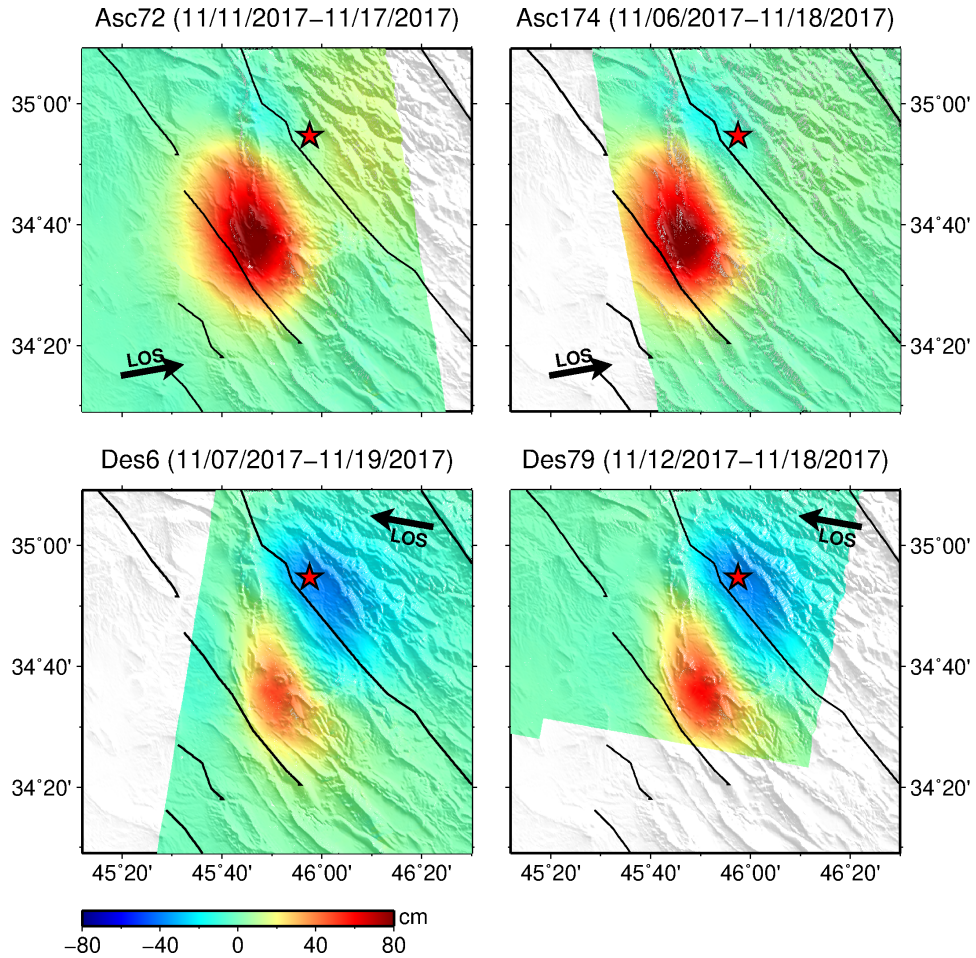
943



944  
 945  
 946 **Figure 1.** Tectonic setting of the 2017 Mw 7.3 Sarpol-e Zahab earthquake. Black line represents  
 947 the active faults in this area. Red star indicates the epicenter of the mainshock. Black beach balls  
 948 represent the locations and focal mechanisms of  $M \geq 4.5$  earthquakes, from 1976-2017  
 949 (<https://www.globalcmt.org>). Inset shows the tectonic setting of the study area. Solid circles  
 950 represent the  $M > 4$  aftershocks catalogued by U.S. Geological Survey (USGS) during ~5 months  
 951 after the mainshock, colored by the time since the mainshock. White boxes denote the ground  
 952 coverage of the Sentinel-1 images from different tracks (only two sub-swaths covering the  
 953 epicenter areas are shown for each track). The red dashed line represents the approximate location  
 954 of the Mountain Frontal Flexure, a topographic and structural relief step that divides the Zagros

955 mountain range from its foreland to the southwest (Emami et al., 2010). AR=Arabian plate;  
956 IN=Indian plate; EU=Eurasian plate; AF=Africa plate.

957



958

959 **Figure 2.** LOS coseismic displacements due to the November 12, 2017 Sarpol-e Zahab earthquake.

960 Positive values correspond to surface motion toward the satellite. Red star represents the epicenter

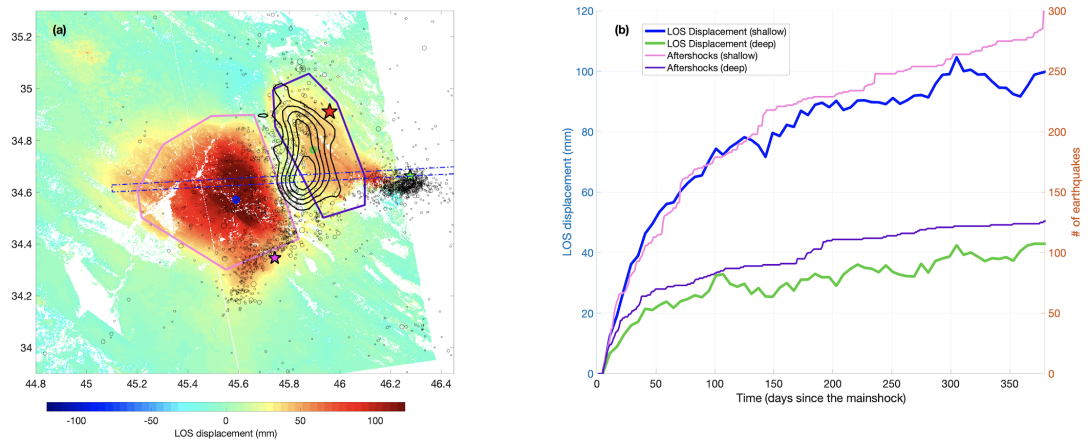
961 of the Mw 7.3 mainshock determined by the U.S. Geological Survey. Black lines denote the faults

962 with dominantly thrust motion in this area. Labels on top of each panel show the acquisition dates

963 of the SAR images used to form the interferograms.

964

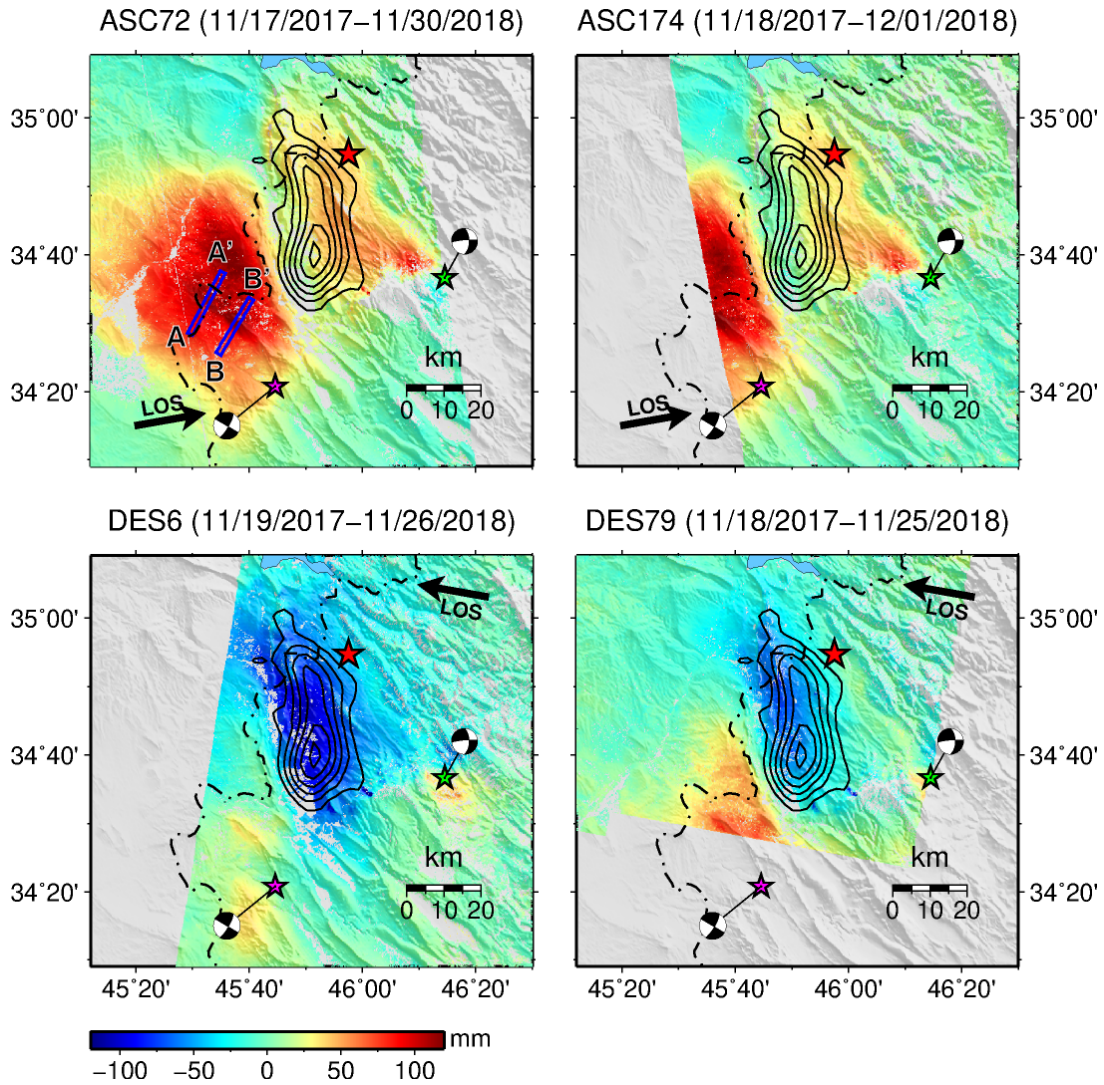
965 To reduce the noise due to atmospheric perturbations and orbital inaccuracies, we flatten the LOS  
966 displacements of each track by removing a linear trend that depends on both local topography and  
967 coordinates  
968



969  
970 **Figure 3.** (a) Cumulative LOS displacement one year after the 2017 Iran-Iraq earthquake, derived  
971 from the Sentinel-1 data of the ascending track ASC72. Black circles represent the aftershocks of  
972  $M > 2.5$  during the same time period from Iranian Seismological Center (<http://irsc.ut.ac.ir/>). Green  
973 and magenta stars denote the epicenters of the two largest aftershocks on 08/25/2018 and  
974 11/25/2018, respectively. Black contours denote the coseismic slip model at 1-m intervals, starting  
975 at 1 m. Polygons in pink and purple represent the areas for which the aftershock temporal  
976 evolutions are shown in (b). (b) temporal evolution of postseismic deformation and cumulative  
977 number of aftershocks updip and downdip of the mainshock rupture. Blue and green curves  
978 represent the postseismic LOS displacements at point A (updip) and B (downdip), respectively.  
979 Magenta and yellow curves represent the cumulative numbers of aftershocks within the updip and  
980 downdip polygons in (a). We correct for the atmospheric noise with Common-Scene-Stacking

981 (Tymofyeyeva and Fialko, 2015). No temporal evolution function or smoothing is applied when  
982 solving for the postseismic deformation time series.

983



984

985

986 **Figure 4.** Cumulative postseismic LOS displacements from four Sentinel-1 tracks. Dates of

987 first and last image acquisitions used are shown on top of each panel. Since CSS has poorer

988 performance in correcting for atmospheric noise of images at the two ends of the catalog, we

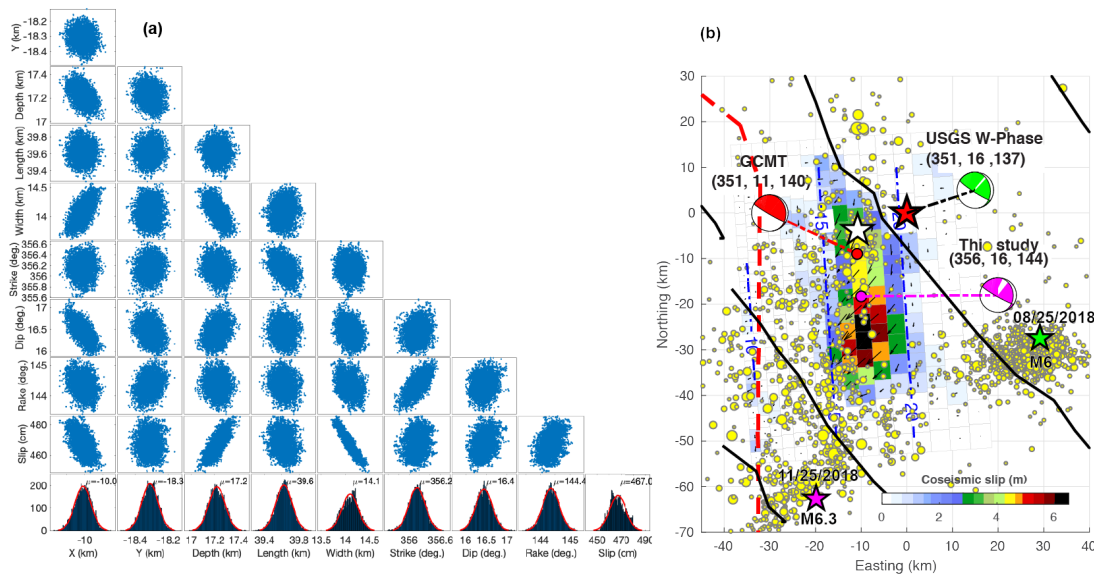
989 discarded the last few scenes to determine the postseismic deformation, although the processed

990 data extend until the end of January, 2019. Positive values correspond to surface motion toward

991 the satellite. Black contours represent the coseismic slip model with slip larger than 1 m, at 1 m

992 intervals. Red, green and magenta stars represents USGS epicenters of the Sarpol-e Zahab Mw 7.2  
 993 mainshock on 11/12/2017, the Mw 6.0 aftershock on 08/25/2018 and the Mw 6.3 aftershock on  
 994 11/25/2018, respectively. Blue boxes in (a) show the profile locations for which the LOS  
 995 displacement time series are shown in Figure 10. Note that the first postseismic image of all four  
 996 satellite tracks was acquired about 5 days after the mainshock and within less than 2 days of one  
 997 another.

998



999

1000

1001 **Figure 5.** Inversion of fault geometry and slip distribution of the 2017 Sarpol-e Zahab earthquake.

1002 (a) Distribution of model parameters in the inversion for fault geometry assuming a single

1003 rectangular slip patch. Locations (eastward X, northward Y and Depth) represent the center of the

1004 rectangular dislocation with respect to the epicenter at 34.911N, 45.959E. (b) Coseismic slip model

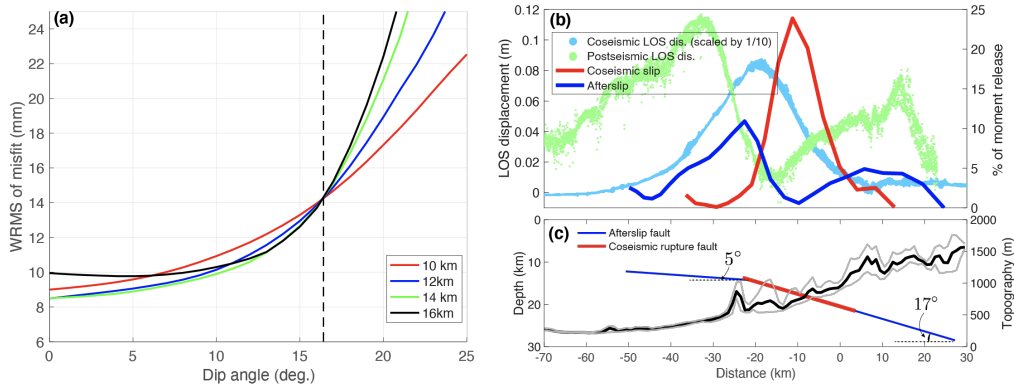
1005 of the 2017 Sarpol-e Zahab earthquake. Yellow circles denote the aftershocks of M>3 till

1006 12/03/2018 from the Iranian Seismic Center (ISC) (<http://irsc.ut.ac.ir/>). Numbers above beach balls

1007 represent the strike, dip and rake angles of the rupture. Dashed blue lines represent depth contours

1008 of the fault plane in km and the red dashed line is the approximate location of the Mountain Frontal  
1009 Flexure (see Figure 1).

1010



1011

1012 **Figure 6.** Optimization of updip fault geometry and comparison of surface displacements

1013 due to coseismic rupture and afterslip. (a) Root-mean-square (RMS) of data misfit as a function of

1014 dip angle of the shallow afterslip fault plane in the inversion of afterslip. Colors represent different

1015 ‘transition’ depths above which the dip angle is allowed to vary from that of the coseismic rupture.

1016 The dip angle below the ‘transition’ depth is fixed at 17 degrees (dashed line). (b) LOS

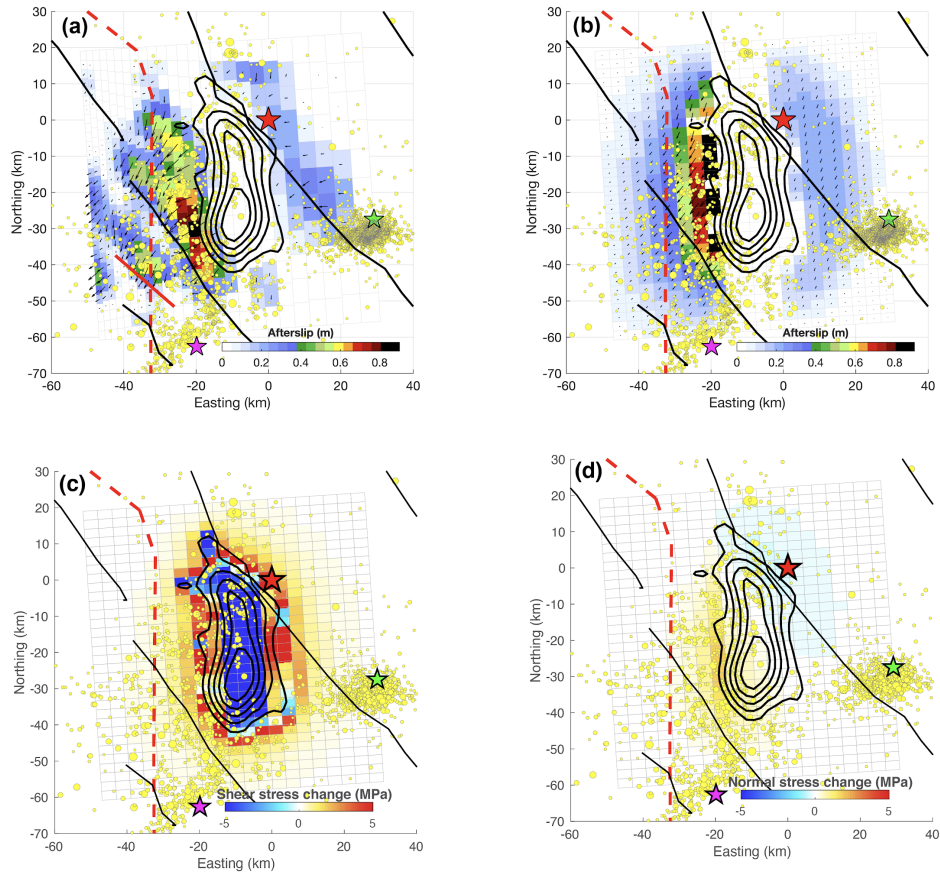
1017 displacements of the ascending track ASC72 (lightblue: coseismic/10, green: postseismic) and

1018 percentage of moment release due to coseismic slip (red) and afterslip (blue) along a profile

1019 perpendicular to the coseismic rupture. (c) cross-section of fault geometry for coseismic rupture

1020 and afterslip. Red and blue lines delineate the coseismic and afterslip segments, respectively.

1021



1022  
1023

**Figure 7.** Afterslip models from (a) kinematic inversion of postseismic deformation, and (b)

1024

stress-driven afterslip simulation assuming a rate-strengthening fault friction. Note that because

1025

the first postseismic SAR image was acquired on 11/17/2017, both models shown here do not

1026

include afterslip during the first 5 days after the mainshock. Panels (c) and (d) show the shear

1027

(along the coseismic slip direction) and normal stress changes (positive for unclamping) produced

1028

by the coseismic rupture, respectively. Yellow circles represent  $m > 2.5$  aftershocks (from ISC

1029

catalog) during the InSAR observation period. Red, green and magenta stars denote the USGS

1030

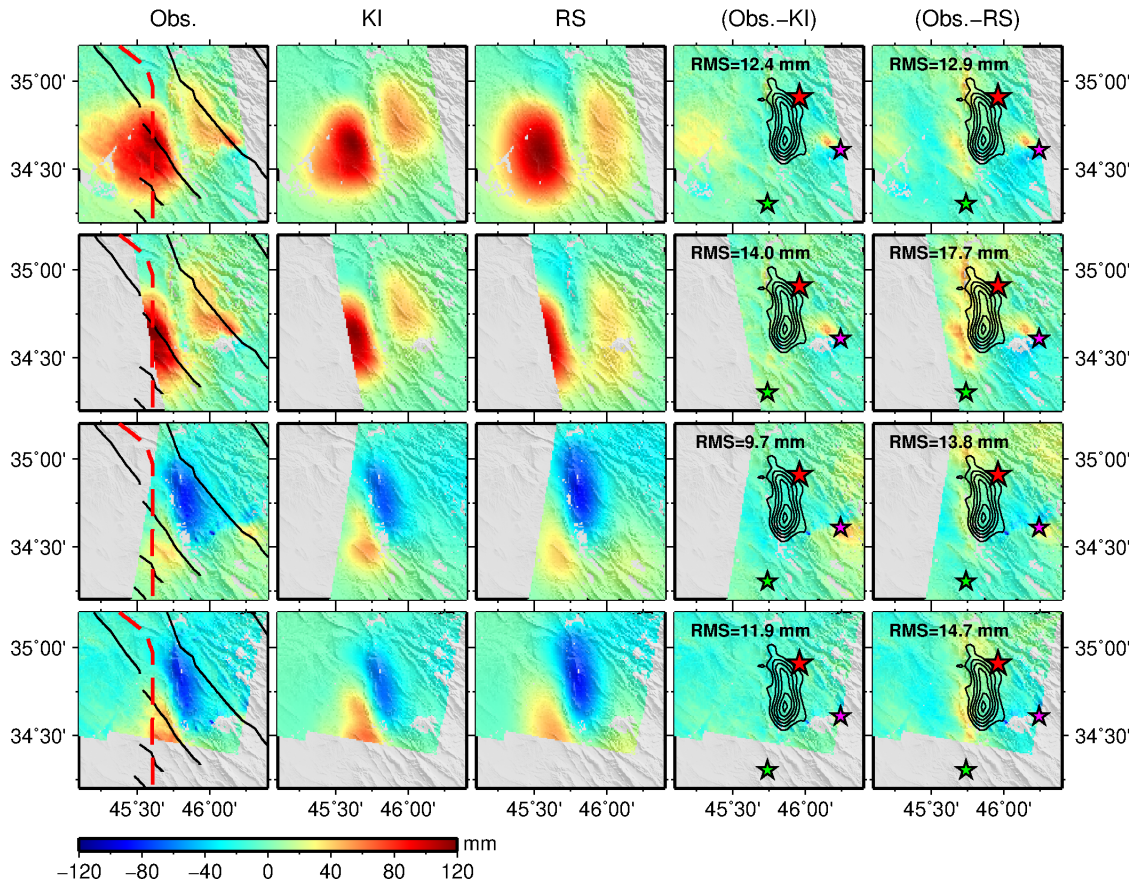
epicenters of the Mw 7.3 mainshock on 11/12/2017, the Mw 6.0 aftershock on 08/25/2018, and

1031

the Mw 6.3 aftershock on 11/25/2018, respectively. Solid red line in (a) denotes the surface trace

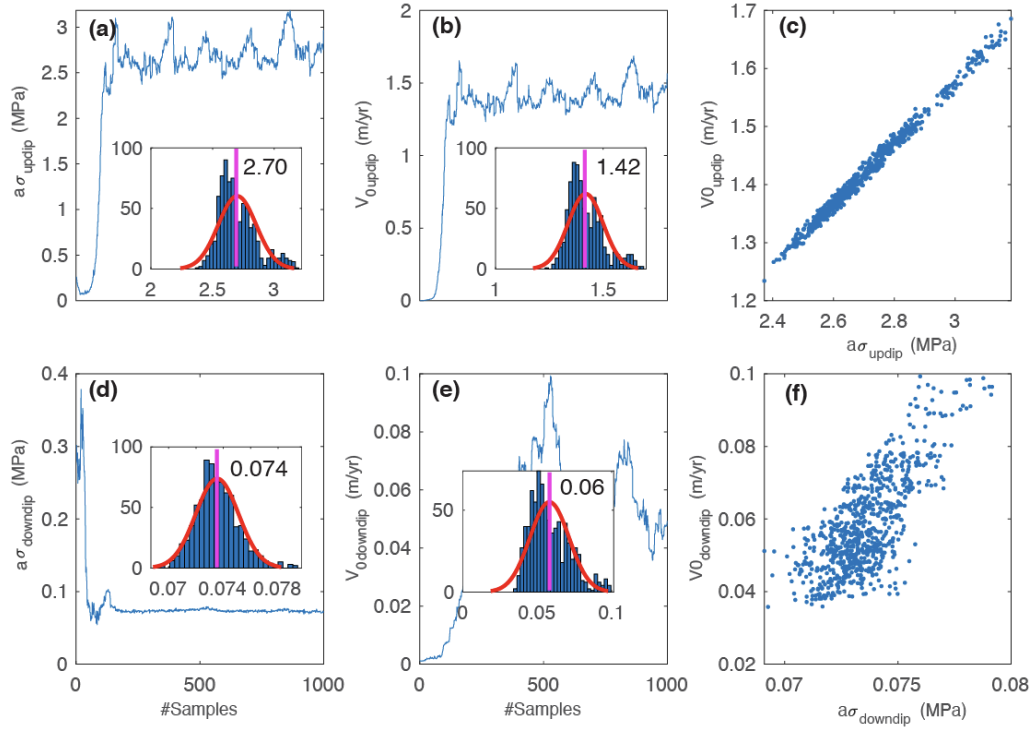
1032

across which both coseismic and postseismic deformation exhibit sharp offsets (Figure 10).



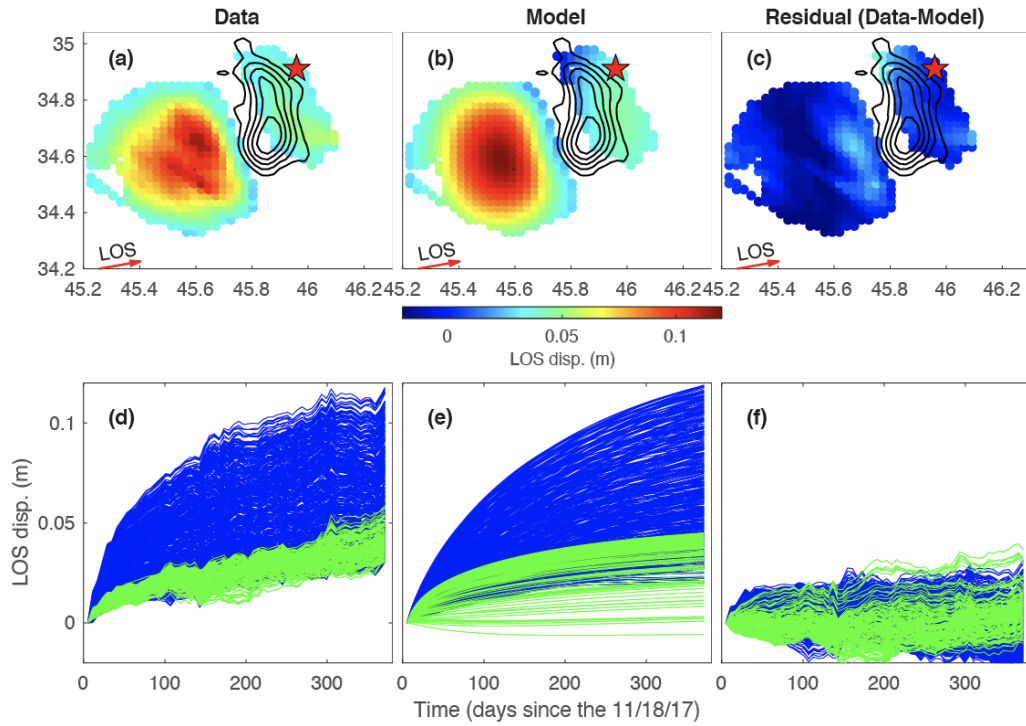
1033  
1034

1035 **Figure 8.** Comparison of cumulative surface displacements between observations and the  
 1036 kinematic inversion (KI) and rate-strengthening (RS) model predictions. Observation periods for  
 1037 each track are the same as shown in Figure 4. Red, magenta and green stars in the last two columns  
 1038 denote the USGS epicenters of the Mw 7.3 mainshock, the Mw 6.0 aftershock on 08/25/2018, and  
 1039 the Mw 7.3 aftershock on 11/25/2018, respectively. Numbers in the last columns show the RMS  
 1040 of misfit at downsampled data points. Black contours represent the coseismic rupture.

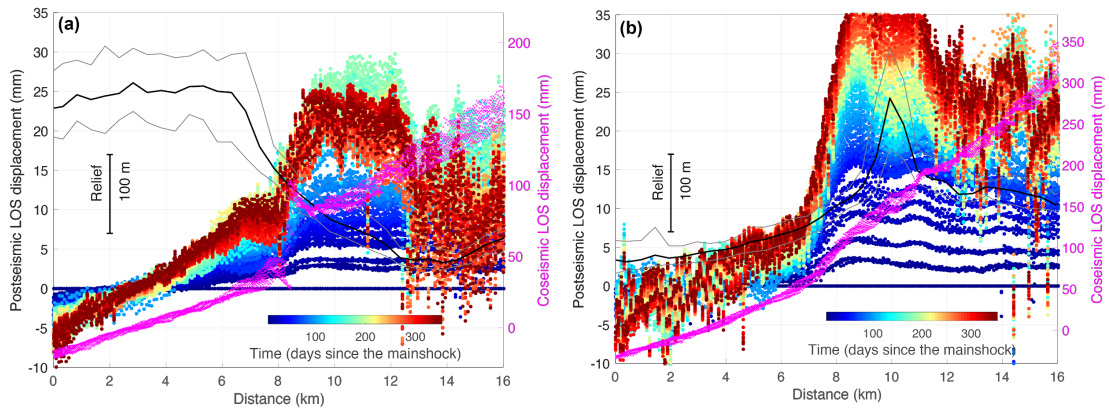


1041  
 1042 **Figure 9.** Sampling histories and distributions of model parameters in the afterslip simulation for  
 1043 fault patches updip ((a) and (b)) and downdip ((d) and (e)) of the coseismic rupture. The correlation  
 1044 between and are shown in (c) and (f). Inserts in each panel shows the histogram of the  
 1045 corresponding parameter after 200 burn-in samples. Red curves represent the best-fitting normal  
 1046 distributions of samples after burn-in, and are labeled with their mean values.

1047



1048  
 1049 **Figure 10.** Comparison of surface deformation between observations and model predictions for  
 1050 the ascending track ASC72. (a-c): cumulative LOS displacements larger than 3 cm after  
 1051 downsampling. Red star denotes the epicenter of the mainshock. (d): Observed (e) modeled, and  
 1052 (f) residual time series of LOS displacements at all downsampled points. Grey and red curves  
 1053 represent the time series at locations updip and downdip of the coseismic rupture, respectively.  
 1054



1055  
 1056 **Figure 11.** Surface creep across secondary faults southwest of the 2017 Sarpol-e Zahab earthquake  
 1057 along a profile (a) with coseismic offset and (b) without clear coseismic offset (see location profiles

1058 A and B in Figure 4). Pink dots represent coseismic LOS displacements (for ascending track  
1059 ASC72) along the profile perpendicular to the surface creep. Colored dots are for the postseismic  
1060 creep, with the color representing time since the mainshock. Black solid curve represents the  
1061 surface elevation.

1062

1063